

FABRICATION AND ROBUSTNESS TESTING OF  
SUPERHYDROPHOBIC NANOSTRUCTURED SURFACES FOR  
ENHANCED JUMPING CONDENSATION

by

JEAN H. SACK

B.S., MECHANICAL ENGINEERING  
MASSACHUSETTS INSTITUTE OF TECHNOLOGY, 2013

Submitted to the Department of Mechanical Engineering in Partial Fulfillment of  
the Requirements for the Degree of

MASTER OF SCIENCE IN MECHANICAL ENGINEERING  
at the  
MASSACHUSETTS INSTITUTE OF TECHNOLOGY

JUNE 2015

©Jean H. Sack. All rights reserved.

The author hereby grants to MIT permission to reproduce and to distribute publicly  
paper and electronic copies of this thesis document in whole or in part in any  
medium now known or hereafter created.

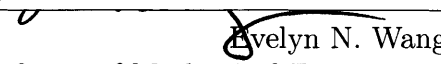
Signature of Author: \_\_\_\_\_

**Signature redacted**

Department of Mechanical Engineering  
May 26, 2015

Certified by: \_\_\_\_\_

**Signature redacted**

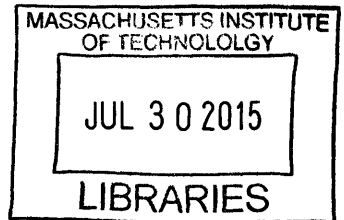
  
Evelyn N. Wang  
Associate Professor of Mechanical Engineering  
Thesis Supervisor

Accepted by: \_\_\_\_\_

**Signature redacted**

  
David E. Hardt  
Professor of Mechanical Engineering  
Chairman, Committee for Graduate Students

**ARCHIVES**





# Fabrication and Robustness Testing of Superhydrophobic Nanostructured Surfaces for Enhanced Jumping Condensation

by

Jean H. Sack

Submitted to the Department of Mechanical Engineering on May 26, 2015  
in Partial Fulfillment of the Requirements for the Degree of  
Master of Science in Mechanical Engineering

## Abstract

Increasing worldwide and domestic demands for power and clean water will require advanced heat transfer materials. Superhydrophobic micro- and nano-structured surfaces which promote a jumping droplet mode of condensation have been shown to enhance heat transfer over conventional filmwise condensation surfaces, but limited robustness testing has been reported validating feasibility of industrial implementation.

This thesis seeks to quantify the robustness of a variety of nanostructures, substrates and coatings by analyzing contact angle measurements and SEM imaging over the course of accelerated robustness testing. This testing was enabled through the design and construction of three custom-built setups intended to accelerate the onset of failure mechanisms. These setups consist of a flow setup to observe resistance to shear flows from internal condensation steam flow, a droplet impingement setup to test mechanical durability, and an elevated temperature condensation chamber to characterize thermal stability. Methods for fabricating nanostructures were also developed, and scalable zinc oxide nanowires (ZnO) and copper oxide nanoblades (CuO) were used. CuO nanoblades were etched into copper, and ZnO nanowires were grown on silicon, low carbon steel, titanium, stainless steel, and electroplated nickel. Hydrophobic coatings tested on these surfaces included stearic acid and two polymer coatings: P2i (40nm) and Semblant.

Observed failure mechanisms were coating degradation and poor nanostructure adhesion. Nanostructure adhesion issues were observed as delamination of ZnO nanowires primarily on stainless steel substrates. Adhesion was improved through the addition of an electroplated nickel layer before nanowire growth, but delamination was still observed. This is likely the result a large mismatch in coefficient of thermal expansion between the ZnO nanowires and the substrate. The etched CuO nanostructures with a fluorinated polymer coating (P2i) showed very little change in performance throughout robustness testing. Characterization methods included contact angle measurements to monitor surface uniformity and durability, and scanning electron microscope (SEM) imaging to observe nanostructure degradation and delamination.

Preliminary work was also done to functionalize the inside of tubes and design a dedicated test setup to characterize heat transfer measurements for internal jumping condensation. This setup will allow for extended robustness testing over a range of temperatures, pressures, and geometries, and give baseline heat flux values for

comparison with dropwise or filmwise internal condensation. While ZnO nanowires still require additional testing and development, CuO nanoblades are good candidates for internal heat transfer measurements and scaled up robustness testing. Assuming this characterization confirms the expected benefits of jumping condensation from increased droplet removal and nucleation density, this technology has the potential to significantly improve power plant efficiency and output worldwide.

Thesis Supervisor: Evelyn N. Wang

Title: Associate Professor of Mechanical Engineering

## Acknowledgments

I would like to thank my thesis supervisor, Professor Evelyn N. Wang, for her attention to detail, high expectations of rigor, and guidance. I have developed greatly from her input, and understand much more of what goes into meaningful scientific research.

During this project, I recieved significant help from labmates in the device research laboratory. I would like to thank all of them, especially Dr. Nenad Miljkovic for serving as my UROP advisor and mentor when I was introduced to the project. Without his wisdom and encouragement, I would not have considered attending graduate school. Another key person responsible for my success is Dr. Dion Antao, for helping me every step of the way, keeping project expectations high, and general good humor. Thank you also to Dr. Banafsheh Barabadi for ideas and careful SEM and FIB analysis, and to Mr. Daniel Preston for additional SEM imaging, valuable discussions, and insightful feedback. Thank you to Dr. Sungwoo Yang for significant contributions in developing the nanostructure synthesis methods used in this work, and to Mr. Jeremy Cho for solving my image analysis crisis when I was running out of time. I would also like to thank Dhananjai Saranadhi for excellent work on the design of the closed loop condensation setup as a thesis student, and Francesca Schembri for her care in sample fabrication as a UROP, which was enormously helpful. I have learned a tremendous amount from everyone in the laboratory, and for this I am forever grateful.

I am incredibly fortunate to have the unwavering support of my parents, Karen and Gary, and my brother Ivan. Their thoughtfulness, work ethic, intellect and sense of adventure has inspired me to work hard, have fun, and explore all that this world has to offer. Finally, thank you to Charlie Wheeler for his unconditional love and support, and for helping me enjoy the challenges of graduate school. He has made my life wonderful, and I thank him for opening my eyes to how magical this world can be.

This research was funded by the Electric Power Research Institute (EPRI), NSF, and Office of Naval Research with Dr. Mark Spector as program director. Imaging was performed at the Harvard Center for Nanoscale Systems, funded by NSF grant ECS-0335765.

# Contents

<b>1</b>	<b>General Motivation</b>	<b>1</b>
1.1	Wetting Dynamics . . . . .	1
1.2	Modes of Condensation . . . . .	3
1.2.1	Filmwise Condensation . . . . .	3
1.2.2	Dropwise Condensation . . . . .	3
1.2.3	Jumping Condensation . . . . .	3
1.3	Codes and Standards . . . . .	4
1.3.1	Condenser heat load . . . . .	6
1.3.2	Ambient environmental conditions . . . . .	6
1.3.3	Turbine backpressure and steam quality . . . . .	6
1.3.4	Steam purity and non-condensable gases . . . . .	6
1.3.5	Air-side cooling . . . . .	6
1.3.6	Tube materials and geometry . . . . .	7
1.3.7	Tube fouling . . . . .	7
<b>2</b>	<b>Selection, Fabrication, and Economic Feasibility of Nanostructures, Substrates, and Hydrophobic Coatings</b>	<b>9</b>
2.1	Nanostructure Synthesis Methods . . . . .	9
2.1.1	Aerogels . . . . .	10
2.1.2	Growth or Chemical Vapor Deposition . . . . .	10
2.1.3	Chemical Etching . . . . .	12
2.2	Intrinsically Hydrophobic Surfaces . . . . .	15
2.3	Hydrophobic Coatings . . . . .	15
2.3.1	Polymer Coatings . . . . .	15
2.3.2	Self-Assembled Monolayer Coatings . . . . .	16
2.4	Selection of Nanostructure, Substrate, and Coating Combinations for Testing . . . . .	17
2.5	Economic Feasibility . . . . .	19
<b>3</b>	<b>Robustness Test Setups and Conditions</b>	<b>21</b>
3.1	Flow Robustness Setup . . . . .	21
3.2	Drop Impingement Setup . . . . .	23
3.3	Accelerated Condensation Setup . . . . .	25

<b>4</b>	<b>Results of Robustness Testing</b>	<b>27</b>
4.1	Robustness Testing Rounds and Schedules . . . . .	27
4.2	Robustness Characterization . . . . .	28
4.2.1	Contact Angle Measurement . . . . .	29
4.2.2	Error Analysis . . . . .	32
4.3	Robustness Characterization Results . . . . .	32
4.3.1	Flow Setup Robustness Results . . . . .	33
4.3.2	Drop Impingement Results . . . . .	34
4.3.3	Accelerated Condensation Results . . . . .	38
4.4	Robustness Conclusions . . . . .	43
<b>5</b>	<b>Closed Loop Internal Condensation Setup</b>	<b>45</b>
5.1	Design Criterion . . . . .	45
5.2	Mechanical System Components . . . . .	46
5.2.1	Boiler and Reservoir . . . . .	46
5.2.2	Test Section . . . . .	46
5.2.3	Chiller . . . . .	47
5.2.4	Sensors . . . . .	47
5.3	Closed Loop Internal Condensation Setup: Next Steps . . . . .	48
<b>6</b>	<b>Conclusions and Future Work</b>	<b>49</b>
6.1	Summary of Work . . . . .	49
6.2	Future and Ongoing Work . . . . .	50

# List of Figures

1-1	Wenzel (a), Cassie-Baxter (b), and partially wetting (c) modes on a nanostructured surface. . . . .	2
1-2	Images of jumping condensation with two drops (a) coalescing (b) before jumping off the surface (c) and (d). Images courtesy of D. Preston [25]. . . . .	4
1-3	Rendering of an air cooled condenser (a), schematic of internal jumping condensation (b). Images: J. Queeney, D. Preston, D. Antao. . . . .	5
2-1	Typical results of ZnO grown on stainless steel without electroplated nickel (a), electroplated nickel on stainless (b), and ZnO growth on electroplated nickel on stainless (c). SEM credit for (a): D. Preston. . . . .	11
2-2	Copper oxide (CuO) nanoblades etched into a copper substrate (a), and CuO etched into electroplated copper on stainless steel (b). . . . .	12
2-3	Electroplating setup with oxygen free high conductivity (OHFC) copper being plated onto an electroplated nickel layer on a stainless steel substrate. . . . .	13
2-4	Stainless steel samples with electroplated nickel and copper before (a) and after copper oxidation (b). Discoloration on samples in (a) are the result of uneven copper deposition during electroplating. . . . .	14
2-5	SEM images of CuO nanoblades before coating (a), after polymer coating (P2i) (b), and FIB cross section image with polymer coating covering the nanoblades (colorized green) under a protective platinum layer (c). SEM images of ZnO nanowires before coating (d) and after polymer coating (P2i) (e). Image credits for (a),(c), and (d): B. Barabadi. . . . .	16
3-1	Schematic of flow setup to simulate shear stresses from steam flow in internal condensation ACC tubes. . . . .	22
3-2	Schematic of drop impingement setup to simulate the impact of water drops on superhydrophobic surfaces according to ACC geometry. . . . .	23
3-3	Schematic of accelerated condensation setup to determine effects of elevated temperatures and pressures for extended continuous condensing periods. Water return and steam inflow lines are connected to a boiler. . . . .	25
3-4	Images of flow setup (a), drop impingement setup (b), and accelerated condensation setup (c). Samples were tested over the course of two weeks with contact angle measurements taken periodically. . . . .	26

4-1	Evolution of contact angles for drop injection and withdrawal for CuO with polymer coating (P2i) after one week of drop impingement testing.	29
4-2	Example of typical scattering (a) using a micro-goniometer on a superhydrophobic surface. Once a drop pins on a defect site (b) the resulting drop growth (c) and evaporation (d) only results in contact angle hysteresis. The base diameter of drops and length of white bars ( $\approx 15\mu\text{m}$ ) in (b-d) are the same. . . . .	30
4-3	Custom micro-goniometer setup used to obtain contact angles. The camera images advancing and receding contact angles as a drop is injected onto the sample with the syringe pump and then pulled back.	31
4-4	Images of the contact angle measurement using FAMAS software for (a) advancing and (b) receding contact angles after three days of accelerated condensation testing. The sample displayed has polymer coated (P2i) ZnO nanowires on a stainless steel substrate with a nickel adhesion layer. After the interface (green line) is drawn, the image processing splines (faint pink lines) measure the contact angle. . . . .	31
4-5	Flow setup advancing contact angle measurements over 1 week (168 hours). Each data point is the averaged value over multiple measurements on different locations on the sample. A polymer coating from P2i was used for all samples. Error bars represent 95% confidence intervals. SEM credits: B. Barabadi, D. Preston. . . . .	33
4-6	Second round drop impingement advancing contact angle measurements for 2 weeks (336 hours) of testing. A polymer coating from P2i was used for all samples. Error bars represent 95% confidence intervals. Left SEM credit: B. Barabadi. . . . .	34
4-7	Final drop impingement testing round for CuO on copper and stainless steel (a), and ZnO on stainless steel with and without a nickel layer (b). Advancing (subscript a, solid line) and receding (subscript r, dashed line) contact angle measurement data. A polymer coating from P2i was used for all samples. Error bars represent 95% confidence intervals.	35
4-8	SEM images of polymer coated (P2i) CuO on stainless steel after 168 hours (a), and CuO on copper after 260 hours (b) of drop impingement testing. . . . .	36
4-9	SEM images of ZnO on stainless steel after one week of drop impingement testing, demonstrating the only nanostructure degradation observed in this test setup. . . . .	36
4-10	SEM images of ZnO on stainless steel with electroplated nickel after 168 hours (a) and after 260 hours (b) of drop impingement testing, both with a polymer coating from P2i. . . . .	37
4-11	Advancing contact angle measurement data for accelerated condensation setup for a total of 2 weeks (336 hours) of testing over 19 days. A polymer coating from P2i was used for all samples. Error bars represent 95% confidence intervals. SEM image credits: D. Preston. . . . .	38

4-12	Final accelerated condensation testing round for CuO on copper and stainless steel (a), and ZnO on stainless steel with and without a nickel layer (b). Advancing (subscript a, solid line) and receding (subscript r, dashed line) contact angle measurement data. A polymer coating from P2i was used for all samples. Error bars represent 95% confidence intervals. . . . .	39
4-13	SEM images before (a,c) and after (b,d) two weeks of accelerated condensation testing for CuO on Copper (a,b) and ZnO on stainless steel with nickel layer (c,d), all with polymer coating (P2i). . . . .	40
4-14	Representative SEM images of polymer coated (P2i) CuO nanoblades on copper (a) and ZnO nanowires on: silicon (b), titanium (c), low carbon steel (d), electroplated nickel (e), and stainless steel (f), after accelerated condensation testing. CuO on copper and ZnO on silicon and on stainless steel with nickel are imaged after two weeks of testing, the rest are imaged after one week of testing. SEM credit (c) and (d): B. Barabadi. . . . .	41
5-1	Schematic (a) and CAD render (b) of closed loop internal condensation setup. . . . .	45
6-1	SEM images of a bare copper substrate (a), after coating with a polymer coating from P2i (b), and after 168 hours of accelerated condensation testing (c). . . . .	51



# List of Tables

1.1	Relevant parameters for the design of robustness tests for steam-side heat transfer surfaces in a 500MW ACC. . . . .	5
2.1	Investigated substrate, nanostructure, and coating combinations. . . .	18
2.2	Estimated costs for specified combination of substrate and nanostructure.	19
2.3	Estimated costs for CuO nanostructures on specified substrates. . . .	20
2.4	Estimated costs for ZnO nanostructures on specified substrates. . . .	20
4.1	Duration of robustness tests and dry times before measurements (hours).	28
4.2	Contact angles for initial impingement testing. . . . .	34
4.3	Contact angles for initial condensation testing. . . . .	38
4.4	Coefficients of thermal expansion for relevant materials. . . . .	42
4.5	Investigated substrate, nanostructure, and coating combinations, and general performance. Materials are copper (Cu), 316 stainless steel (SS), nickel (Ni), carbon steel (CS), titanium (Ti), and silicon (Si). .	43



# Chapter 1

## General Motivation

Considering oil, coal, nuclear, hybrid natural gas, and concentrated solar power, over 60% of US electricity and over 80% of world electricity is produced using heat cycles and steam condensers.[1] Improved heat transfer across the condensing surface allows for constant turbine output with a reduced steam inlet temperature. This improves cycle efficiency by minimizing heat energy into the boiler, and enables more feasible use of air cooled condensers (ACC), which provide less effective external cooling. Typical condenser materials, made from steel, stainless steel, titanium, or in rare cases, copper,[2] have high surface energies resulting in filmwise condensation.[3] Surface functionalization is expensive with limited research confirming robustness. Therefore almost all industrial steam condensers use these materials as is for the condensing surface, accepting the poor heat transfer performance.[4, 5, 2] One method of improving this performance is by decreasing the surface energy on the condensing surface with a hydrophobic coating.[6, 7] To evaluate feasibility of industrial implementation, current wear and failure mechanisms must be understood and addressed with final surfaces and coatings proven sufficiently robust to warrant the added expense in manufacturing and maintenance.

In this chapter, an overview of general wetting dynamics, condensation modes, and standard operating conditions and geometry for an ACC are provided in sections 1.1, 1.2 and, and 1.3, respectively.

### 1.1 Wetting Dynamics

Condensation modes are differentiated through the equilibrium of energies between liquid and substrate. Droplets will arrange themselves in the orientation of lowest energy, which for smooth surfaces is governed by Young's equation,

$$\gamma_{SL} + \gamma_{LV}\cos\theta = \gamma_{SV}, \quad (1.1)$$

where  $\gamma$  is the surface tension between solid (S), liquid (L) and vapor (V).[8, 9] For a smooth surface, the contact angle,  $\theta$  defines whether a surface is hydrophilic ( $\theta < 90^\circ$ ) or hydrophobic ( $\theta > 90^\circ$ ).[9] When surface roughness is introduced, the possible contact angles can be expanded to include superhydrophilic ( $\theta \simeq 0^\circ$ ) and

superhydrophobic ( $\theta > 150^\circ$ ). These angles can be calculated with corrections for the roughness, depending on the permeability of the liquid between the structures.[10] If the liquid wets through the roughness, as displayed in Figure 1-1a, it is classified as Wenzel wetting where the contact angle is

$$\cos\theta_W = r\cos\theta, \quad (1.2)$$

and  $r$  is the total surface area/projected area.[11]

Alternatively, if droplets contact only the nanostructured tips (Figure 1-1b), the interaction is classified as Cassie-Baxter wetting.[12] In this case, the contact angle is

$$\cos\theta_C = f_1\cos\theta + f_2, \quad (1.3)$$

where  $f_1$  and  $f_2$  are the area fractions of the material ( $f_1 + f_2 = 1$ ).

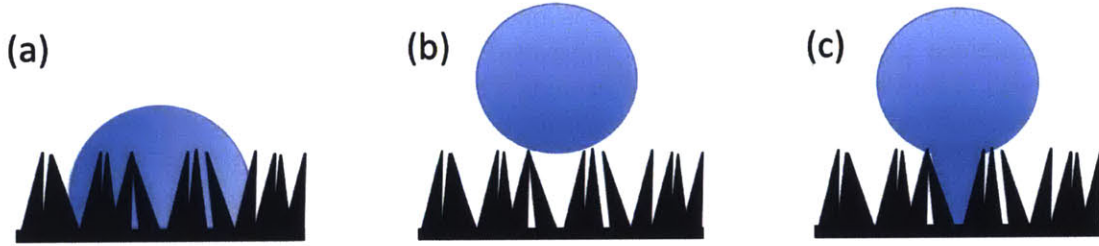


Figure 1-1: Wenzel (a), Cassie-Baxter (b), and partially wetting (c) modes on a nanostructured surface.

Contact angle measurements are obtained by imaging the angle between a drop and a surface at the 3-phase contact point. For this work, advancing and receding contact angles were monitored, which are taken while the contact area of the drop base with the surface is expanding and contracting, respectively. These measurements are typically done with drops below the capillary length, where surface tension effects dominate over gravitational effects.

These forces are equally important at the capillary length,[9] which is calculated from

$$l_{cap} = \sqrt{\frac{\gamma_{LV}}{\rho g}}. \quad (1.4)$$

With gravity  $g = 9.81 \text{ m/s}^2$ , and properties of water at STP of surface tension,  $\gamma_{LV} = 72.8 \text{ mJ/m}^2$ , and density,  $\rho = 998 \text{ kg/m}^3$ , the capillary length of water is 2.73 mm. As a drop increases in size, gravitational and body forces dominate and drops deform and move according to the gravitational field. This causes drops to flatten, making it more difficult to use curve fitting around the shape to determine contact angles. Contact angle techniques are discussed in detail in section 4.2.1.

## 1.2 Modes of Condensation

Three modes of condensation are discussed in this section. It includes the two commonly observed condensation modes, filmwise and dropwise condensation, as well as the novel jumping droplet condensation mode which is the focus of this project.

### 1.2.1 Filmwise Condensation

Metallic surfaces have high surface energies making them intrinsically hydrophilic and wetting.[3] When used in condenser applications, the high attraction between the liquid and surface results in a film of water forming, referred to as filmwise condensation.[4] This film of water inhibits heat transfer by being thermally insulating, and by requiring significant film thickness accumulation before gravitational effects can result in removal.[4]

### 1.2.2 Dropwise Condensation

If the surface energy can be reduced, it is possible to induce dropwise condensation with enhanced heat transfer through increased droplet nucleation density and mobility, and reduced droplet departure size.[4] This mode, with a 5-7 $\times$  heat transfer improvement over filmwise condensation, can be achieved by functionalizing the surface with a hydrophobic coating, such as a long-chain fatty acid,[13, 14, 15, 16, 17] wax,[11] or polymer coating.[6, 7] Drops are removed by gravity when the droplet exceeds the capillary length of water. With the use of internal flow condensation geometry and droplet sweeping from vapor shear forces, heat transfer of up to 600 kW/m<sup>2</sup> on hydrophobic surfaces have been reported.[18, 19] Other methods of enhancing heat transfer, such as oil-infused surfaces and bi-philic surfaces have also been investigated, but are not considered for this work.[20, 21]

### 1.2.3 Jumping Condensation

If a surface is roughened with nanostructures of appropriate length scale before the hydrophobic coating is applied, jumping droplet condensation can be achieved.[22] This third mode of condensation has the potential for up to 30% improved heat transfer over state of the art dropwise condensation. This is achieved at low supersaturations, where supersaturation is defined as the ratio of vapor pressure of the environment to the saturation pressure at the condensation surface temperature.[23, 24] Small drops, 10-100  $\mu\text{m}$  in diameter, nucleate on the tips of the nanostructures, and jump off the surface due to a release in surface energy upon coalescence, as shown in Figure 1-2.[25] Some of this energy is converted to kinetic energy which results in motion of the merged droplet perpendicular to the condensing surface, while the rest is dissipated by viscosity during coalescence and subsequent droplet oscillation.[22, 26]

Jumping condensation is most effective when drops exhibit a partially wetting mode, as seen in Figure 1-1c.[27] Partially wetting droplets are favored for their excellent heat transfer and mobility; suspended Cassie-Baxter drops can jump but have

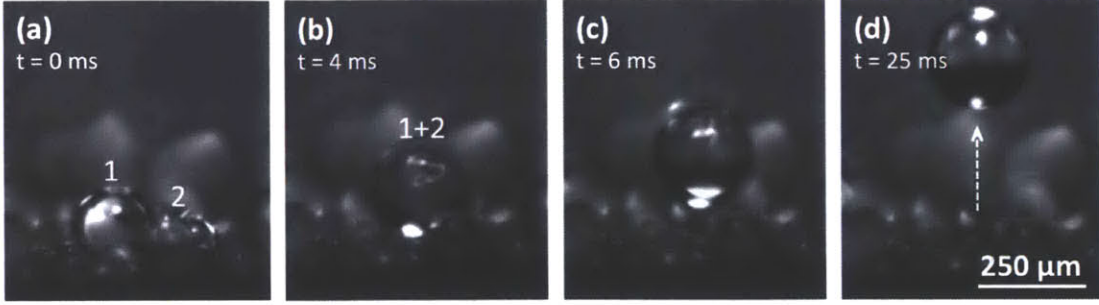


Figure 1-2: Images of jumping condensation with two drops (a) coalescing (b) before jumping off the surface (c) and (d). Images courtesy of D. Preston [25].

much slower growth, and wetting Wenzel droplets must rely on gravitational force for removal.[28] This wetting morphology requires nanostructure or surface structure geometries no larger than  $0.5\text{-}2\ \mu\text{m}$ , and can be predicted through a dimensionless energy ratio

$$E^* = \frac{\cos\theta_{CB}}{\cos\theta_W} = -\frac{1}{r\cos\theta_a}, \quad (1.5)$$

where  $\theta_{CB}$  and  $\theta_W$  are the advancing contact angles for the Cassie-Baxter and Wenzel droplet morphologies, respectively.[27] For  $E^* > 1$ , Wenzel droplet morphologies are favored, while for  $E^* < 1$ , partially wetting droplets should emerge.[27] In addition, the distance between nuclei of droplets should be  $2\text{-}5\times$  the spacing between the structures to achieve jumping condensation.[27, 29] If the supersaturation is increased, the increased nucleation density can cause droplets to coalesce at the base of the nanostructures, reaching a flooded state with 41% lower heat transfer than dropwise surfaces.[23] At a flooded state, droplet nucleation density is too high to sustain partially wetting drops, resulting in the transition to Wenzel drops which merge into a film.[26]

### 1.3 Codes and Standards

The enhanced heat transfer from hydrophobic dropwise or superhydrophobic jumping condensation is appealing for industrial steam condensers. Air cooled condensers (ACC) are an especially interesting application because of the lower external cooling available from air, compared to traditional direct cooling with water. Since jumping droplet condensation is more effective at heat removal than filmwise condensation, it is predicted that the condensation temperature can be reduced by around  $10^\circ\text{C}$  for the same heat load.[30] The smaller droplet removal size, enabling entrainment in the steam flow, may also help reduce the pressure drop through the condensation tubes. Together, these effects could improve plant efficiency by up to 3%, saving around \$7.5M annually.[31] A render of a proposed A-frame ACC design is provided in Figure 1-3.

A large part of determining the feasibility of implementation is demonstrating robustness over time under expected or accelerated conditions. Therefore, codes and

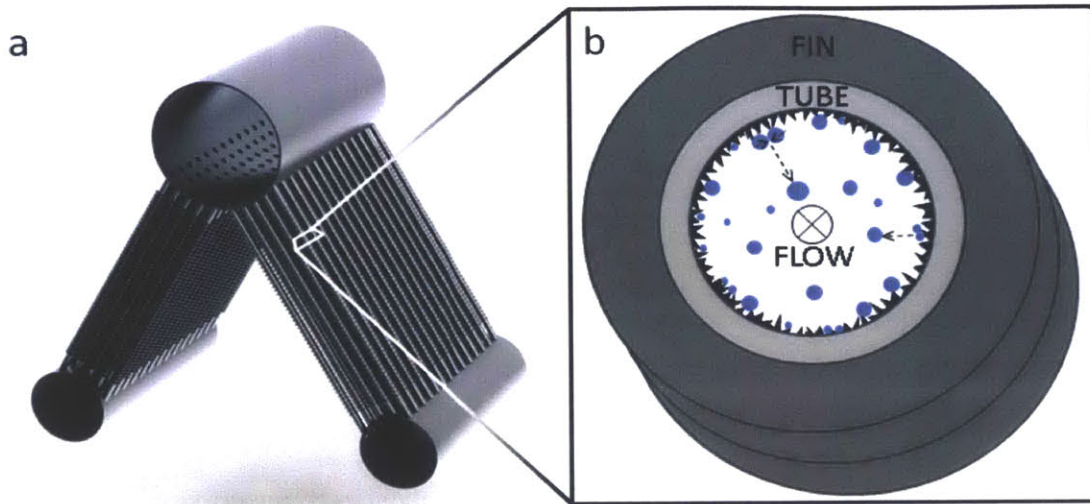


Figure 1-3: Rendering of an air cooled condenser (a), schematic of internal jumping condensation (b). Images: J. Queeney, D. Preston, D. Antao.

standards were reviewed to create relevant robustness tests under reasonable conditions for a ACC, with standards affecting the steam-side heat transfer surfaces compiled in this section. The ACC components not considered in detail include the condenser support structure, steam ducting, condensate receiver tank, fan design and associated driving systems, air removal system, maintenance access, and instrumentation and controls to monitor the overall system. A summary of the main design conditions (operating conditions or standards) is tabulated in 1.1.

Table 1.1: Relevant parameters for the design of robustness tests for steam-side heat transfer surfaces in a 500MW ACC.

Parameter	Value
Condenser heat load (MW)	732.68
Inlet temperature difference, ITD ( $^{\circ}\text{C}$ ) <sup>1</sup>	14 to 21
Air temperature ( $^{\circ}\text{C}$ )	-18 to 43
Steam flow (kg/s)	5.25
Turbine exit steam quality	0.92 to 0.987
Turbine back pressure (kPa)	6.8 to 27
Steam contamination level (ppb)	< 2
Dissolved non-condensable gases (oxygen, ppb)	< 20
Air flow (kg/s)	49100
Air inlet velocity (m/s)	< 5
Tube orientation ( $^{\circ}$ )	50 to 70
Tube fouling resistance ( $\text{m}^2\text{K}/\text{W}$ )	0.0005

In the following sub-sections, specifics of the standards are provided based on the different aspects of the ACC design, *i.e.*, heat transfer, geometry, water, *etc.*

### 1.3.1 Condenser heat load

The condenser heat load in a 500 MW coal fired power plant is about 732.68 MW.[32] This requires a potential ACC footprint of 7,580-12,786 m<sup>2</sup>,[32] depending largely on the ambient environmental conditions, temperature, and the desired operating turbine backpressure.

### 1.3.2 Ambient environmental conditions

Plants are assumed to be at sea level, with a typical ambient annual average temperature at an arid southwest site of 18°C.[5] This allows for an average year-round condensation temperature of 43°C while maintaining an inlet temperature difference (ITD)<sup>1</sup> of 24°C.[5] There is a considerable range for all of these values from best day to worst day. Expected ambient temperatures range from -18°C to 43°C with a maximum expected condensation temperature of 64°C.[32] Designs can expect a minimum ITD of 14°C, with a maximum ITD of 25°C.[5]

### 1.3.3 Turbine backpressure and steam quality

For the above listed environmental operating conditions, a turbine exhaust quality of 0.95, a steam flow of 315 kg/s and a turbine backpressure around 12 kPa are expected.[32] However, the turbine exhaust quality can range from 0.92 to 0.987 and while the backpressure can be as favorable as 6.8 kPa it cannot exceed 27 kPa for worst day operation (hottest days of summer, dry-bulb temperature ~ 43°C) to avoid mechanical and metallurgical damage.[5, 33]

### 1.3.4 Steam purity and non-condensable gases

High purity steam is required to prevent damage to the turbine, and minimize corrosion on the inside of steam tubes. Steam can be expected to have less than 2 parts per billion (ppb) of sodium, chloride and sulfate, and anion concentration below 0.2 µS/cm.[2] Current practices elevate condensate pH to 9.0-9.6, depending on whether units are composed of copper alloys, to further minimize corrosion.[2] Non-condensable loads must be removed to avoid 'dead zones' with decreased heat transfer area. Dissolved oxygen up to 50 ppb can be expected in condensate but should be maintained at a value below 20 ppb. This can be achieved (during steady, normal operation) using a vacuum deaerator, and preventing air leakage into the condensate.[34]

### 1.3.5 Air-side cooling

Ambient temperature cooling airflow is assumed to be 49,101 kg/s with  $35.4 \times 10^6$  alpm<sup>2</sup>, and is provided by 72 fans 8.5-10 m in diameter.[32][5] Typical fans have 4

---

<sup>1</sup>The ITD is the difference between the steam condensation temperature (for an ACC) and the ambient dry-bulb temperature

<sup>2</sup>Actual liters per minute (alpm) are volumetric gas flow rates in a system independent of density

blades operating at 110 rpm. More blades and lower motor speed (rpm) can be used for low noise operation, but results in significant air-side pressure losses.[5, 34] Air inlet velocities are generally less than 5 m/s.[34]

### 1.3.6 Tube materials and geometry

Steam condenser tubes can be made from carbon steel, stainless steel, titanium, copper alloys and brass.[2] Externally galvanized carbon steel, however, is the only material specifically associated with ACC finned tubes.[5] Tubes are welded at an angle of 50-70° between a steam duct at the top of the system, and water collection and return pipe at the bottom, as seen in Figure 1-3.[35] Tube thickness is minimized to decrease tube thermal resistance, but must be structurally capable of sustaining a maximum design working pressure of 160 kPa and temperature of 121°C.[34] External fins made from either aluminum or galvanized steel are spaced 1.5 to 2.5 mm apart to allow surface cleaning.[5] These fins must be capable of withstanding over 5.2MPa from high pressure cleaning water to minimize performance degradation due to external fouling.[34]

### 1.3.7 Tube fouling

A typical fouling factor of  $F = 0.0005 \text{ m}^2\text{K}/\text{W}$  should be assumed for the steam and air side fouling. This factor affects the overall heat transfer coefficient as  $1/U_{service} = 1/U_{clean} + F$ , and can be designed around by increasing steam flow rate.[34]



## Chapter 2

# Selection, Fabrication, and Economic Feasibility of Nanostructures, Substrates, and Hydrophobic Coatings

Nanostructures enhance the natural wetting characteristics of surface materials.[10] Since metals have high surface energies and are naturally wetting, uncoated metal oxide nanostructures are superhydrophilic and wick water through the structures. When hydrophobic coatings are applied, however, the hydrophobicity of the coating is enhanced by the surface roughness and the surfaces become superhydrophobic. From previous work and laboratory tests it was determined that zinc oxide (ZnO) nanowires and copper oxide (CuO) nanoblades are suitable for enabling partially wetting droplets at a small enough diameter for jumping condensation. There are many other possible nanostructures, some of which are discussed in section 2.1, but CuO and ZnO were selected for ease in manufacturing and potential for scalability, as discussed in section 2.1. A variety of conformal hydrophobic coatings also have potential, as detailed in section 2.3, but few of these have been proven robust for more than a few days of testing. Finally, the results of an investigation into the cost of implementing superhydrophobic surfaces on an industrial scale is provided in section 2.5.

### 2.1 Nanostructure Synthesis Methods

Nanostructures with the potential for superhydrophobic behavior can be categorized based on three main synthesis methods: aerogels, growth or chemical vapor deposition, and chemical etching. Currently, jumping condensation has been demonstrated on grown ZnO nanowires and etched CuO nanoblades. Fabrication methods, with the benefits and drawbacks of each created nanostructure, are summarized for aerogels in section 2.1.1, grown structures in section 2.1.2 and etched structures in section 2.1.3.

### 2.1.1 Aerogels

One method of applying nanostructures is through the use of aerogels. The first step in the synthesis of aerogels is through low-temperature (typically  $T < 100^{\circ}\text{C}$ ) traditional sol-gel chemistry using different types of chemical precursors, such as salts.[36, 37] Unlike most wet gels, aerogels are then created through supercritical drying of a metal oxide (inorganic) or carbon based gel (organic) on a substrate. Depending on the specific method, nanospheres, nanofibers, 2-D membrane, and monolith morphologies on top of the desired metal substrate are possible.[38] Consequently, the product is highly porous, has a very large surface area, and has highly robust and stable thermodynamic and chemical properties.[39] Carbon aerogels are mainly achieved through pyrolysis of organic aerogels (usually at  $T > 500^{\circ}\text{C}$ ), and while they can be intrinsically hydrophobic (when annealed at higher temperatures) they have low thermal conductivity.[40] Aerogels also can suffer from poor mechanical robustness in thick layers with the specific concern of delamination due to the thermal and mechanical stress formation.[38, 39]

### 2.1.2 Growth or Chemical Vapor Deposition

Another method of nanostructure creation is growth or chemical vapor deposition (CVD). This technique relies on the application a seed layer on the substrate, either through solution or vapor deposition, which can be grown into nanostructures. There are many possible combinations of oxide nanostructures and substrates which exhibit excellent jumping droplet condensation characteristics, but the reliance upon adhesion of the seed layer to the substrate causes concerns with delamination and wear. Zinc oxide nanowires have been shown to exhibit good jumping, with titanium oxide nanostructures providing a similar length scale.[41, 42, 24]

#### Zinc Oxide Fabrication

The first step in creating ZnO nanowires is preparing the seed solution, which is methanol based with equal parts 0.01M zinc acetate dihydrate and 0.03M sodium hydroxide, heated to  $60^{\circ}\text{C}$  for two hours with stirring, in a silicone oil bath. Potential samples can be made from a variety of possible substrates, including stainless steel, carbon steel, titanium, silicon, and glass. These samples are solvent cleaned with acetone, ethanol, isopropyl alcohol, and DI water and dried with compressed nitrogen or air. Then they are plasma cleaned with oxygen to remove organic compounds from the surface. The seed layer is applied through a series of seed and methanol rinses, separated by nitrogen or argon drying steps. Care must be taken to apply the seed layer and dry samples as uniformly and gently as possible, to avoid displacement or patterns of seeds on the surface, which can lead to irregular nanowire growth. Samples are then gradually heated to  $350^{\circ}\text{C}$ , annealed for 20 minutes, and slowly cooled to room temperature. They are then immersed upside down at an angle in a water based solution with equal parts 0.025M zinc nitrate and 0.025M Hexamethylenetetramine at  $90^{\circ}\text{C}$  for 3 hours. Finally, samples are carefully removed, rinsed and gently dried.

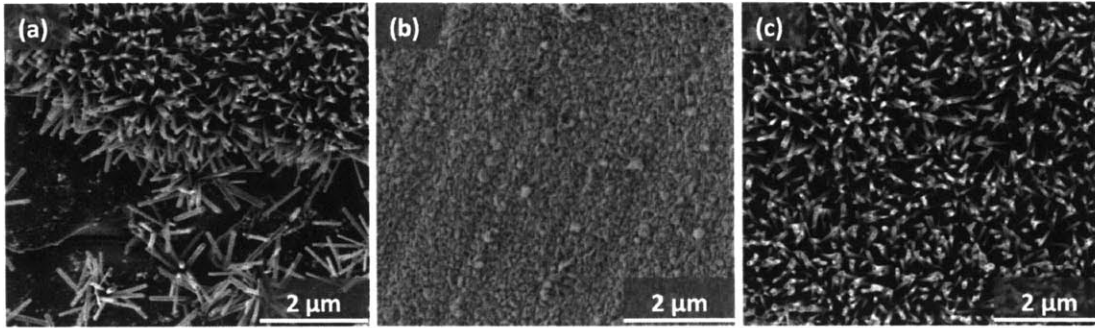


Figure 2-1: Typical results of ZnO grown on stainless steel without electroplated nickel (a), electroplated nickel on stainless (b), and ZnO growth on electroplated nickel on stainless (c). SEM credit for (a): D. Preston.

The process of growing ZnO nanowires on stainless steel surfaces is erratic, with over half of samples grown in any batch unusable due to barren patches on the order of a few  $\mu\text{m}^2$  or larger. These patches reveal large, smooth grains separated by grain boundary cracks, as can be seen in the bottom half of Figure 2-1a. A highly magnified SEM image of the hexagonal ZnO crystals is provided in Figure 2-5(d)

### Nickel Adhesion Layer

In addition to frequently poor growth uniformity on metallic substrates, initial robustness tests showed that ZnO structures have poor adhesion, especially to stainless steel, and delaminated during tests. Metallic surfaces are passivated by oxide layers or foreign contaminants, which limits bonding capabilities.[43] Therefore, an electroplated nickel adhesion layer can be used to activate the surface and improve adhesion between materials.[43] It is especially useful when bonding materials to 316 stainless steel, because of the highly passivating chromium oxide layer that forms on the surface.[44] The nickel electroplating procedure is done using a highly acidic solution which removes this oxide layer, temporarily activating the stainless steel surface and allowing the nickel to bond. Since the nickel oxide layer is not as resistant to corrosion, it allows for a more effective bond with the nanostructures. With the added nickel adhesion layer, 9 out of the 10 samples created appeared uniform as determined through SEM imaging as shown in Figure 2-1c.

Samples are prepared for electroplating by solvent cleaning, plasma cleaning, and immersion in hydrochloric acid. These steps must be done very thoroughly, as any residue left on the sample can prohibit nickel adhesion. Then samples are submerged in a nickel plating solution on a titanium rack cathode, with a nickel depolarized electrolytic anode. The solution is gently stirred and a cell current of 40-50  $\text{mA}/\text{cm}^2$  is applied for around 7 minutes. Small bubbles appear on the sample throughout the process, and though samples visually appear the same once removed, an adherent layer is applied. This setup is shown in Figure 2-3, except with a deep teal colored solution and silver colored anode for nickel plating. An SEM image of electroplated nickel is provided in Figure 2-1b, showing a uniform surface with roughness on order

of a few hundred nm. Solution is Technic ‘Woods Nickel Strike’ and contains nickel chloride concentrate, hydrochloric acid and DI water.[45] Specific make-up details available by request from Technic Inc.

### 2.1.3 Chemical Etching

A final method considered for creation of nanostructures uses highly acidic or basic solutions, with or without electricity, to etch the surface of metal. Copper oxide nanoblades, tungston oxide nanowires, and anodized aluminum oxide nanopillars are some of the structures possible with this method.[23, 46, 47] These structures demonstrate excellent robustness, chemical and thermal stability, and good hydrophobicity, either intrinsically, or with the application of a coating.[46, 47] Since the etched nanostructures are part of the substrate itself instead of adhered independently, these surfaces exhibit excellent durability.

#### Copper Oxide Fabrication

To manufacture CuO nanoblades, oxygen-free 110 type Copper samples are solvent cleaned, dried with compressed nitrogen or air, and submerged in a 2M hydrochloric acid solution for 30 seconds to remove the natural oxide layer. Then the samples are immersed in a solution of sodium chlorite, sodium hydroxide, trisodium phosphate dodecahydrate and DI water at 95°C for 8 to 10 minutes with stirring. Once samples are removed, they are immediately rinsed with water, dried, and left on a hot plate at 80°C for an hour. With samples too large for horizontal immersion in the glassware available, a slightly altered vertical method can be used. In this case, copper tube samples are placed in a graduated cylinder immersed in a beaker of boiling water to maintain temperature as pre-heated solution added. The procedure is then followed as above. During the oxidation process, the samples go from a bright copper color to a completely black matte surface, as shown in Figure 2-4. SEM images showing the delicate blades are provided in Figure 2-2 and Figure 2-5 a, b, and c.

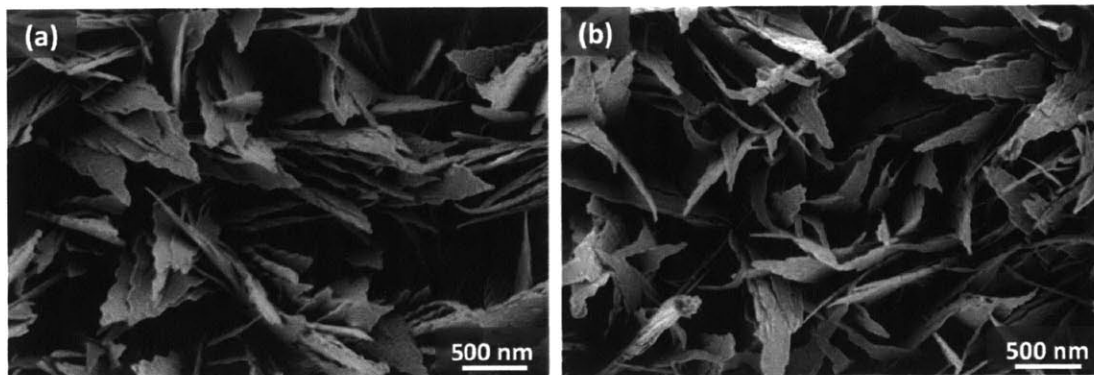


Figure 2-2: Copper oxide (CuO) nanoblades etched into a copper substrate (a), and CuO etched into electroplated copper on stainless steel (b).

One challenge with this procedure is maintaining the solution temperature at 95°C, without it boiling or cooling too much when samples are added or removed. If the solution is cooled too much, the samples will not etch uniformly, resulting in an incomplete oxidation.

### Copper Oxide Fabrication for Non-Copper Substrates

CuO nanoblades are desirable for excellent demonstrated jumping performance and durability, but industrial condensers avoid the use of copper because of the expense of bulk copper, concerns of corrosion, and concerns of copper particulates spreading throughout the steam cycle. Therefore, it is of interest to demonstrate CuO performance and durability when used in conjunction with other metals.

For this process, an electroplated nickel layer is applied as detailed previously. Then a similar procedure can be followed to electroplate copper metal onto the surface. Samples are placed on a titanium rack immersed in a copper plating solution with stirring at room temperature, as seen in Figure 2-3.

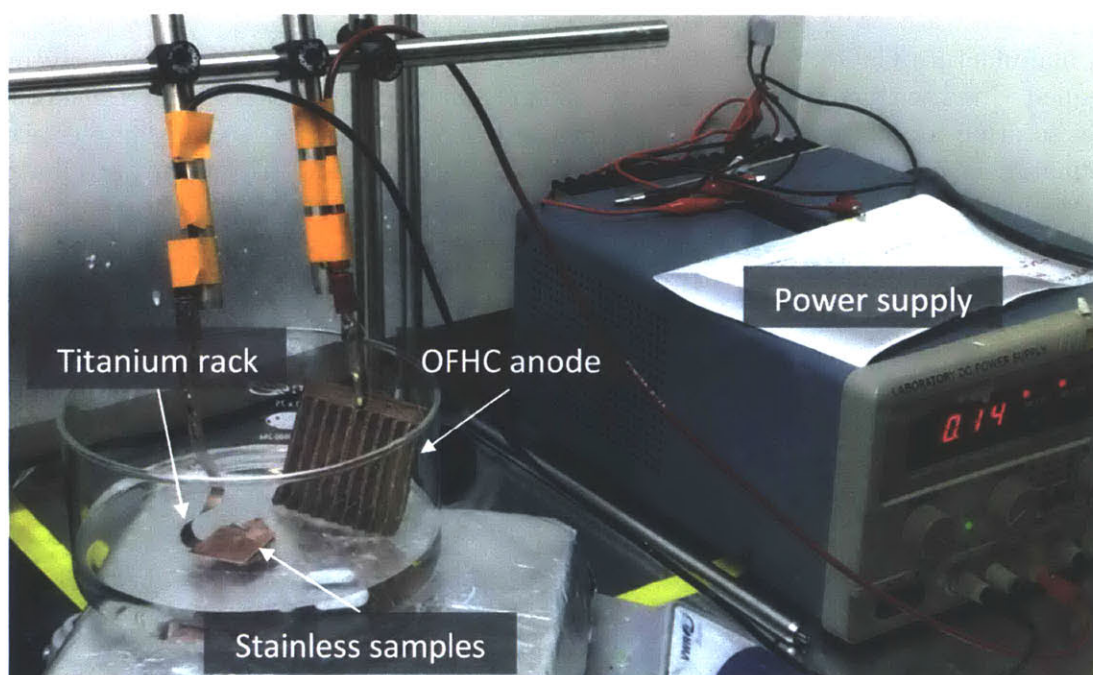


Figure 2-3: Electroplating setup with oxygen free high conductivity (OFHC) copper being plated onto an electroplated nickel layer on a stainless steel substrate.

Oxygen free high thermal conductivity (OFHC) copper anodes are connected to a cell current of 10mA/cm<sup>2</sup>. The plating process produces around a  $\mu\text{m}$  of copper in 10 minutes, which immediately turns the sample a light copper color. Technic ‘Copper-Cyanide’ contains potassium cyanide, potassium copper cyanide, potassium hydroxide, copper “C” brightener, rochelle salts and DI water.[48] Specific make-up

details available by request from Technic Inc.<sup>1</sup>

The result of etching on the electroplated surface is comparable with the CuO blades directly on a copper substrate, as shown in Figure 2-2b. The copper application was somewhat inconsistent, and was likely a result of non-uniform field lines in the electroplating process.[49] The copper ions are distributed according to length of these lines, resulting in faster, thicker deposition on the surfaces closest to the anode, which appeared as darkened roughness on the samples, as seen in Figure 2-4.[49] For surfaces further away from the anode which plated more slowly, the copper layer appeared more uniform and bright, as seen on the sample to the right in Figure 2-4.

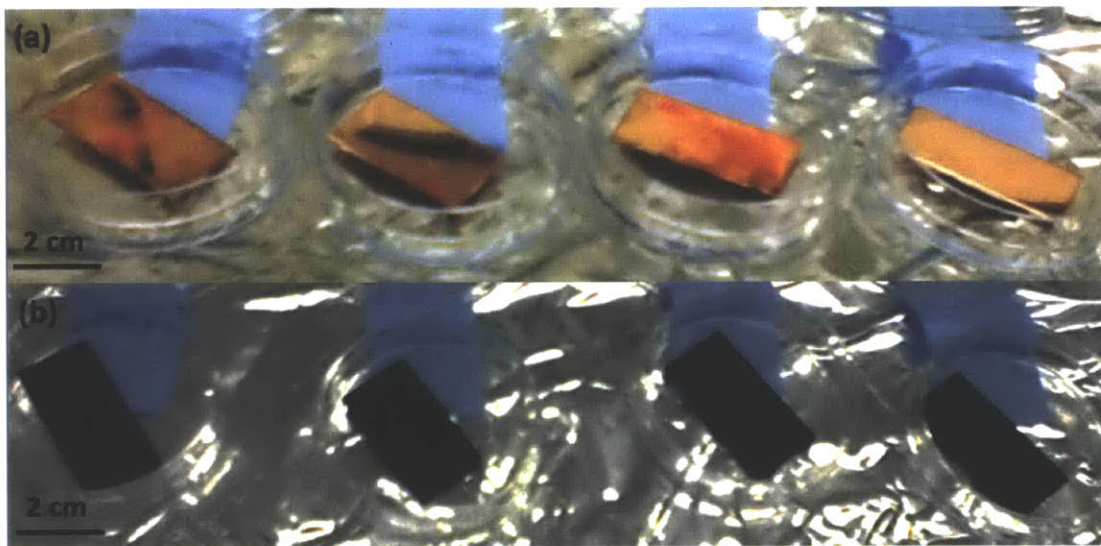


Figure 2-4: Stainless steel samples with electroplated nickel and copper before (a) and after copper oxidation (b). Discoloration on samples in (a) are the result of uneven copper deposition during electroplating.

Regardless of anode proximity, all electroplated layers remained intact when laboratory tape was applied to the sample face and then pulled off.<sup>2</sup> These irregularities did not visually affect the final oxidized surface, which all appear uniform in Figure 2-4, but may have resulted in decreased mechanical strength, accounting for somewhat poorer performance than CuO on a fully copper substrate in robustness testing. For future fabrication, a lower current density should be considered to allow for a slower, more even deposition.

---

<sup>1</sup>Copper-Cyanide solutions are extremely effective at plating onto hard-to-plate metals such as stainless, but all cyanide based solutions are extremely hazardous and should not be pursued without proper PPE and EHS knowledge. If ‘Copper-Cyanide’ comes into contact with acid, it releases Hydrogen Cyanide gas which can be fatal.

<sup>2</sup>This is a commonly used method to test adhesion of electroplated materials, as suggested by Technic technical support.

## 2.2 Intrinsically Hydrophobic Surfaces

There are two methods of creating intrinsically hydrophobic surfaces that can be used for dropwise condensation. The first method implants H<sup>+</sup>, O<sup>+</sup>, or N<sup>+</sup> ions into a metal surface forming nanoscale roughness and chemical heterogeneities produced by particulate precipitates bonded to the metal surfaces.[50] Sustained dropwise condensation has been shown to exist over periods of multiple months, but has been implemented into industry with limited success. Early work with ion implantation applied to an industrial condenser in the Dalian Power Station only exhibited consistent dropwise condensation at low subcooling.[51, 3, 52] The second method is to use a material that favors hydrocarbon absorption, such as noble metals or rare earth oxides.[53, 54, 55] While these methods may produce sufficiently hydrophobic surfaces for dropwise condensation, ion implantation and rare earth oxides significantly increase thermal resistance, and noble metals are prohibitively expensive. Therefore these surfaces are poor candidates for industrial scale implementation.

## 2.3 Hydrophobic Coatings

Non-intrinsic hydrophobic coatings suitable for dropwise condensation can be created through the application of low surface energy coatings on smooth metal surfaces. When applied over surfaces with the required roughness, it is possible to create superhydrophobic surfaces with a water contact angle of 150° to over 170°. Coatings themselves generally have poor thermal conductivity, and completely water repellent coatings are too limiting on nucleation sites for heat transfer improvements. Uniform thin or monolayer coatings that succeed in prevent wicking through the nanostructures have been shown to exhibit excellent jumping condensation.

### 2.3.1 Polymer Coatings

There are many brand-name, patented polymer coatings such as P2i,[56] Semblant,[57] and RainX,[58] that are used for water-repellency. Thin polymer coatings, such as P2i and Semblant, are around 30-60 nm thick and have have exhibited excellent jumping condensation. The P2i polymer coating is applied through a plasma assisted chemical vapor deposition (p-CVD) process, and as discussed in chapter 4, has proved durable for up to two weeks of accelerated testing. SEM images of CuO and ZnO before and after coating with a polymer coating (P2i) are provided in Figure 2-5. Focused ion beam (FIB) milling was also used to provide a cross-section image, showing the coating thickness as a thin halo around the structures, colored green in F igure 2-5c.

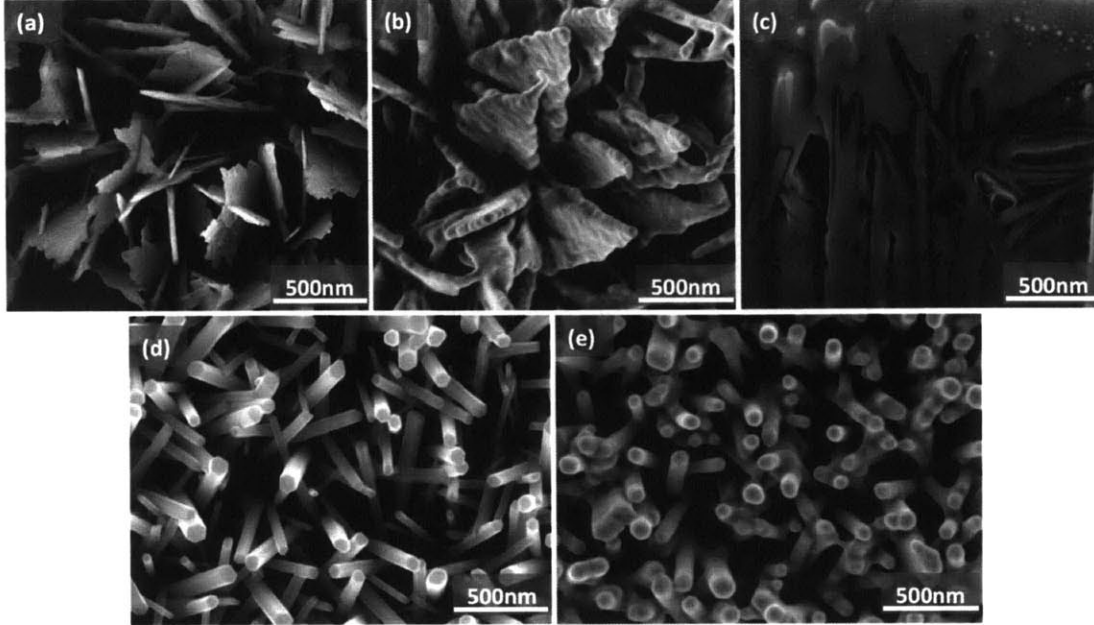


Figure 2-5: SEM images of CuO nanoblades before coating (a), after polymer coating (P2i) (b), and FIB cross section image with polymer coating covering the nanoblades (colorized green) under a protective platinum layer (c). SEM images of ZnO nanowires before coating (d) and after polymer coating (P2i) (e). Image credits for (a),(c), and (d): B. Barabadi.

From this technique and from information provided by P2i, the thickness is estimated to be between 30 and 40 nm. Initiated chemical vapor deposition (iCVD) coatings may also be a potential solution since they display good robustness during continuous condensation over time, but have not been tested for compatibility with jumping condensation.[59]

Other polymer coatings, with a minimum of 500 nm thickness, have been shown to be robust for dropwise condensation for over a year and a half,[60] but are not compatible with roughness length scales required for jumping condensation. In addition, the added thermal resistance through these thicker coatings negates the heat transfer improvement gained from a transition to dropwise condensation.[60] Other coatings such as polytetrafluoroethylene (PTFE), parylene, and silicones have also been demonstrated to enable dropwise condensation.[61]

### 2.3.2 Self-Assembled Monolayer Coatings

Other coating options are self-assembled monolayer (SAM) chemical compounds with long hydrocarbon tails. These include alkanethiols and silane coatings which can render surfaces hydrophobic,[62, 63, 64, 65, 66, 67] or superhydrophobic if compatible with nanostructures.[68] Methods of coating applications include spray,[69, 70] aqueous immersion,[71] or vapor deposition.[59] While significant work has been done on these coatings, however, they have performed poorly for extended testing, based on

prior work and preliminary tests discussed in chapter 4. Thiols have been found to oxidize over short time scales upon exposure to ambient conditions or UV radiation, and reduce to disulfides and sulfonates which can be removed with water.[72] Thiols, or long chain saturated fatty acids, are inexpensive and desirable due to low toxicity and biocompatibility, but also less thermally stable and have weaker bonds than silanes (which rely on covalent bonding), and are therefore a particularly poor choice for higher temperature applications.[13, 14, 15, 16, 17] Even though silanes are more thermally stable, durability is still a major concern with degradation found over the course of 5 consecutive days of testing.[19]

Both silane and thiol coatings, specifically trichloro(1H,1H,2H,2H-perfluorooctyl)-silane and stearic acid,(n-octadecanoic acid,  $CH_3(CH_2)_{16}CO_2H$ ) while not robust, are still useful for heat transfer measurements. They can be applied in a few hours using a hexane immersion method with 2 $\mu$ L of silane per 50 mL hexane, or a 1mM stearic acid in hexane solution. Samples are immersed for 2-48 hours at room temperature and immediately rinsed with acetone and dried with compressed nitrogen. An alternative chemical vapor deposition (CVD) method has also been demonstrated for silane, with 5 minute deposition time followed by one hour heating at 120°C. This CVD method is faster, but often inconsistent or completely ineffective.

## 2.4 Selection of Nanostructure, Substrate, and Coating Combinations for Testing

Through a combination of prior work and literature review, a variety of samples were selected for robustness testing. The first round of tests investigated ZnO on silicon because of good compatibility between nanostructure and substrate, and ease of fabrication. Coatings tested for this round were stearic acid, and the polymer coatings P2i, and Semblant. The results of this testing round, discussed in chapter 4, indicated that the P2i polymer coating was the most stable, and was therefore used exclusively for the rest of tests. For the second round of testing, CuO nanoblades on copper were added, and ZnO nanowires were grown on low carbon steel, titanium, and stainless steel substrates, which are compatible with industrial steam condensers. The results of these tests, also discussed in chapter 4, revealed significant delamination of ZnO nanostructures on all substrates (especially stainless steel), motivating the addition of samples fabricated with an electroplated nickel adhesion layer. In addition, as CuO showed excellent durability, work was done to integrate the nanoblades with different substrates (namely stainless steel), using electroplated copper. Final round testing was then performed with a condensed set of samples. This included CuO on stainless steel with CuO on copper as a control, and ZnO on stainless steel with and without an electroplated nickel layer. The full set of samples tested are summarized in table 2.1.

Table 2.1: Investigated substrate, nanostructure, and coating combinations.

Substrate	Nanostructure	Coating
Silicon	ZnO	P2i (polymer coating)
Silicon	ZnO	Semblant (polymer coating)
Silicon	ZnO	stearic acid
110 Copper	CuO	P2i
Low Carbon Steel	ZnO	P2i
Titanium	ZnO	P2i
316 Stainless Steel	ZnO	P2i
316 Stainless Steel/nickel	ZnO	P2i
316 Stainless Steel/nickel/copper	CuO	P2i

## 2.5 Economic Feasibility

Even with demonstrated durability, industrial implementation is only feasible if economic benefits from improved heat transfer justify the added expense of surface functionalization. If an assumed benefit of operation with jumping-droplet condensation can reduce the steam condensation temperature from 64°C to around 53°C, an expected increase in yearly revenue of around \$7.5M can be expected.[30]

Based on available information, a state of the art dry direct (ACC) cooling system costs approximately \$90 M for a 500-MW coal-fired power plant. This cost includes manufacturing and installation of an ACC at roughly \$1.5 M per cell (60 cells). Based on preliminary ACC design which uses the same tube geometry, the expected cost of nanostructure integration and the alternate tube material used is an additional \$9-18 M as outlined in Table 2.2.

Table 2.2: Estimated costs for specified combination of substrate and nanostructure.

Tube Material	Nanostructure	Estimated Additional Cost (\$)
Stainless Steel (SS)	CuO	9.7M
Stainless Steel (SS)	ZnO	17M
Low Carbon Steel (CS)	CuO	9.0M
Low Carbon Steel (CS)	ZnO	11M
Titanium (Ti)	ZnO	18M
Copper (Cu)	CuO	9.6M

As described in chapter 4, CuO on copper, and ZnO on steel and titanium, proved to be robust over a week of accelerated testing for continuous condensation, liquid flow over the sample and droplet impingement of the surface. Therefore, to accurately determine the length of service, and or the interruption to power production for repair or replacement of the proposed structures/coating, scaled up robustness tests are required.

While the polymer coating (P2i) has been shown to withstand the preliminary accelerated robustness testing, use of this coating will require a custom setup costing around \$3-5M to accommodate 10 m long tubes for a preliminary ACC design. For laboratory scale samples, the cost is \$1000 to coat an area of roughly 0.5 m<sup>2</sup>, though the majority of the cost is due to specific setup and preparation of samples and is expected to be considerably lower for a dedicated system. The hydrophobic coating process is done through plasma-assisted chemical vapor deposition (p-CVD). However, it is unlikely that it will be repairable or rejuvenated without the ACC being disassembled. Therefore, the estimated life cycle cost will potentially involve assembly and disassembly of the ACC in addition to the processing step required for repair/replacement of the coating.

The surfaces and coatings described in this section could also be considered for implementation with other steam condenser technologies, which are considerably less expensive to build than ACC systems. Direct cooling condensers are budgeted at \$4-6M installed for a 500MW plant, and wet cooling towers are budgeted at \$8-10M

installed.[73] The cost of hybrid cooling systems are a weighted average of wet and dry cooling systems, dependent upon heat load assignment for each technology.[73] The minimized pressure drop through tubes that makes jumping-droplet condensation in ACC systems so appealing will not apply to these systems, but enhanced heat transfer will still significantly improve performance. Expense of tube functionalization for these systems will scale with surface area, but otherwise remain consistent with values provided above. A specific breakdown of costs from best estimates of bulk pricing online is provided in tables 2.3 and 2.4

Table 2.3: Estimated costs for CuO nanostructures on specified substrates.

Process	Cost (\$)	CuO/SS	CuO/CS	CuO/Cu
Solvent Clean <sup>1</sup>	2.9M	X	X	X
HCl Clean	1.3M	X	X	X
Cu Electroplating	3.4M	X	X	
Ni Electroplating <sup>2</sup>	5.3M	X		
CuO Integration <sup>3</sup>	1.2M	X		X
Polymer Coating (P2i)	3-5M	X	X	X

Table 2.4: Estimated costs for ZnO nanostructures on specified substrates.

Process	Cost (\$)	ZnO/SS	ZnO/CS	ZnO/Ti
Solvent Clean <sup>1</sup>	2.9M	X	X	X
Ni Electroplating <sup>2</sup>	5.3M	X		
ZnO Integration <sup>4</sup>	8.1M	X	X	X
Polymer Coating (P2i)	3-5M	X	X	X

<sup>1</sup> Solvent cleaning includes costs for chemicals used in the process (acetone, ethanol, isopropyl alcohol and DI water)

<sup>2</sup> Volume of nickel electroplating chemicals assumes solution reuse for 10 tubes

<sup>3</sup> Volume of chemicals for CuO integration assumes reuse for 3 tubes

<sup>4</sup> Volume of chemicals for ZnO integration assumes partial reuse (seed solution only) for 3 tubes

## Chapter 3

# Robustness Test Setups and Conditions

Since enhanced heat transfer was demonstrated for jumping condensation at low supersaturations,[26] a characterization of the thermal and mechanical stability of nanostructures and coatings is required to determine industrial feasibility. Knowledge of specific failure modes of both coating and selected nanostructure is needed to synthesize the most durable surfaces possible. Therefore, custom robustness setups were designed and built to simulate expected industrial conditions in an accelerated manner. Specific items of concern are shear flow of the steam on the superhydrophobic nanostructured surfaces, impingement of drops on the surface after drops coalesce and fall out of the steam flow, and thermal stresses and waterlogging from extended condensation at elevated temperatures and pressures. Details of design and construction are provided for the flow setup in section 3.1, the drop impingement setup in section 3.2, and the accelerated condensation setup in section 3.3.

### 3.1 Flow Robustness Setup

The first setup addresses the shear forces on nanostructures created by the very high flow rate of steam through internal condensation tubes in an ACC. Since testing in an industrial sized setup is not viable, a scaled down system was created to mimic the stresses associated with industrial operation. To most accurately simulate the inside of a tube and ensure uniform flow across each sample, two samples are placed flush with the wall midway down narrow channels, as depicted in Figure 3-1. Water is pumped through the channels at an equivalent Reynolds number to industrial flow. The four channels are merged with tubes and T's to allow for one line through the pump with uniform flow between channels.

Each channel is 0.6 cm wide, 1.2 cm deep, and 38 cm long. The base is made out of white delrin for ease of machinability and chemical stability. The samples are centered at 19 cm to give adequate length for fully developed flow from the inlet to the sample, and past the sample to the exit. Samples are mounted with double sided copper tape on removable stages. These sample holders, as seen in Figure 3-

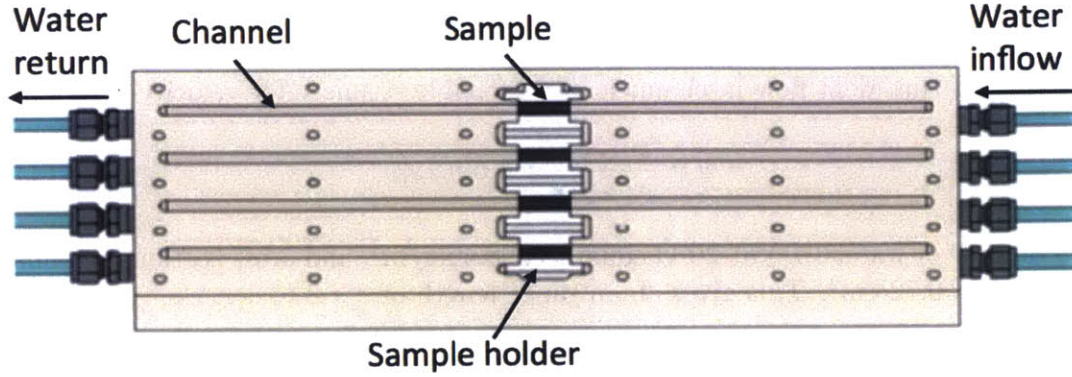


Figure 3-1: Schematic of flow setup to simulate shear stresses from steam flow in internal condensation ACC tubes.

1, are press-fit into cut-outs of the same shape in the channel walls and base. All areas except the channels are covered with a laser cut gasket (McMaster super-soft silicone rubber, 1/8" thick). A laser cut acrylic lid (1/4" thick) is placed over the entire setup, with a hole pattern through the lid and silicon rubber gasket as shown in figure 3-1. Bolts (1/4-20) are passed through these holes and threaded into the delrin with soft rubber washers under flat washers to reduce direct stresses on the acrylic. Water is pumped through the channels with 1/2" swagelok components (1/2" NPT straight pipe fittings, flexible tubing, and swagelok 1/2" Tees) by a 3.3 GPM diaphragm pump (Flojet, Northern Tool). A schematic of the setup showing channels and sample placement is shown in Figure 3-1, and an image of the setup in operation is depicted in Figure 3-4a.

Industrial ACC tube geometry is 0.02 m x 0.2 m, for a hydraulic diameter ( $D_h$ ) of  $4 \cdot A/P = 0.036$  m. Given a steam flow rate of 5kg/s through an ACC cell [32] with 2280 tubes per cell, and a dynamic viscosity of steam ( $\mu_{steam}$ ) at 55°C of  $1.06 \times 10^{-5}$  Pa-s, the Reynolds number for the setup is

$$Re = \frac{4 * \frac{\dot{m}}{tube}}{\mu_{steam} * \pi * D_h} = 7,201. \quad (3.1)$$

This is considered transition flow, as it is between the laminar flow ( $Re < 2300$ ) and turbulent flow regimes ( $Re > 10,000$ ). [4] To optimize space, the hydraulic diameter ( $De$ ) of channels in the laboratory setup are reduced, and water is used to determine resistance to continual immersion. As the Reynolds number is preserved and the accelerated condensation setup is designed to test for resistance to thermal stresses, changing the working fluid from steam to water is expected to be the most destructive test of coating and structure stability. Therefore, the required mass flow rate for one channel, calculated with dynamic viscosity of water at 20°C of  $1 \times 10^{-3}$  kg/(ms), is

$$\dot{m}_{water} = \frac{Re * \mu_{water} * \pi * De}{4} = 0.045[kg/s] = 2.9[L/min]. \quad (3.2)$$

With 4 channels in series, the volumetric flow rate is calculated to be 11.5 L/min.

To verify that flow is fully developed, the entrance length is calculated based on the hydraulic diameter of the channels. Though there are a wide variety of correlations available for turbulent flow in channels, a reasonable estimate for velocity is

$$v = \frac{\dot{m}_{water}}{\rho_w * A_f} = 0.6[m/s], \quad (3.3)$$

with density of water ( $\rho_w$ ) at 20°C equal to 998.4 kg/m<sup>3</sup>, and cross sectional channel area ( $A_f$ ) of 0.72 cm<sup>2</sup>. This gives an entrance length of

$$L_h = 4.4 * Re_{De}^{1/6} * De = 0.085[m]. \quad (3.4)$$

Since the channel length is 38 cm long, this allows any entrance effects to be neglected.

## 3.2 Drop Impingement Setup

Another concern in an industrial ACC is the effect of impinging droplets. These may form from coalescence of jumping droplets in the steam flow, or from pinned drops that could form on defect sites. To simulate these effects, a drop impingement setup was designed and created with a water reservoir and gravity fed needles to create distinct drops. For the first round of testing, a syringe pump was used to produce one drop every 50 seconds which fell 4 cm to impinge on two samples angled at around 30°. Long term, continuous testing on multiple samples with a faster impingement rate was needed, motivating design and construction of dedicated setup for secondary and final testing. As seen in the schematic in Figure 3-2, this setup includes a water reservoir, needle droppers, samples on a baseplate tilted at 60°, and water return line. An image of the final setup in operation is provided in Figure 3-4b.

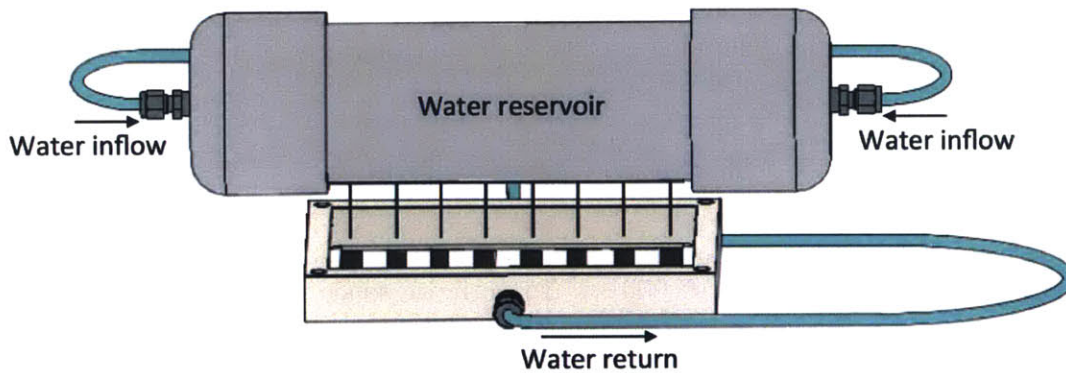


Figure 3-2: Schematic of drop impingement setup to simulate the impact of water drops on superhydrophobic surfaces according to ACC geometry.

Industrial ACC geometries with 2 cm ID tubes angled at 60° [35] determine that the maximum distance drops can fall is  $ID/\cos(60^\circ) = 4$  cm with an associated max-

imum impact velocity of 0.88 m/s. The main expected destructive mechanism is the water hammer pressure. An estimate of the magnitude of the shockwave that results from a water drop hitting a surface, given speed of sound in water of  $c = 1497\text{m/s}$  and density of water at  $20^\circ\text{C}$  of  $\rho_w = 998.4\text{ kg/m}^3$ , is

$$\Delta P \simeq \rho c_{fluid} \Delta v = 1.3[\text{MPa}]. \quad (3.5)$$

This pressure depends only on impact velocity, and is independent of drop size.[74] The shockwave magnitude is on the same order as the reported shear strength between nanowires and substrates (around 1 MPa).[75][76]

The setup uses a PVC reservoir with gage 7 needles (length  $L = 0.0254\text{ m}$ , radius  $R = 0.0019\text{m}$ ) to produce 8 drops in parallel. The calculated drop radius (and therefore expected required pump flow rate) can be modeled as a pendant drop and estimated from a scaled force balance of surface tension and gravity.[9] With water surface tension of  $\gamma = 0.0728\text{ N/m}$  at  $20^\circ\text{C}$ , capillary length of water of  $\lambda_c = 2.7\text{mm}$ , and a scaling factor for the fraction of weight that detaches of  $\alpha = 0.6$ ,

$$R_{drop} = \left( \frac{3 * \lambda_c^2 * R}{2 * \alpha} \right)^{1/3} \quad (3.6)$$

which for our system gives a drop radius of 1.8 mm.[9] For eight drops with volume of 0.15ml every second, the required flow rate is  $Q=1.18\text{ g/s}$ , or  $Q = 71\text{ ml/min}$ . The required pump pressure using eight gage 7 needles is minimal, and is overcome with the hydrostatic pressure in the reservoir. This can be modeled assuming poisseulle flow given dynamic viscosity of water ( $\mu_w$ ) at  $20^\circ\text{C}$  of  $1 \times 10^{-3}\text{ kg/(ms)}$ , flow rate of  $Q = 1.48 \times 10^{-4}\text{ kg/s}$ , and internal needle diameter ( $D$ ) of 0.0038m, as

$$Pressure = \frac{128 * \mu_w * L * Q}{\pi * D^4} * (8\text{needles}) < 6[\text{Pa}]. \quad (3.7)$$

As hydrostatic pressure for a 0.711 m deep reservoir is  $P_{hs} = \rho * g * h = 697\text{ Pa}$ , the pump is only required to circulate the liquid in the system.

Finally, this setup has an impact of 150 drops per minute or 1.5M drops per week on exactly the same location, making it extremely accelerated compared to conditions expected in industry. An estimate for the number of potentially impinging drops during industrial operation is given from

$$n = \frac{q''}{V * \rho * h_{fg}} \quad (3.8)$$

where heat flux  $q'' = 70\text{ kW/m}^2$  with  $4^\circ\text{C}$  of  $\Delta T_{LMTD}$ , drop volume  $V = 8.2 \times 10^{-9}$ ,  $\rho_{water} = 990\text{ kg/m}^3$  at  $45^\circ\text{C}$  (expected condensation temperature), and  $h_{fg} = 2237\text{ kJ/kg}$  for water. This suggests that the length of time for an equivalent number of drops to impinge on a  $1\text{ mm}^2$  area in industry would be around 12 years.

### 3.3 Accelerated Condensation Setup

The final robustness setup is an accelerated condensation setup to characterize the thermal and water-logged robustness of the coated nanostructured surfaces. It allows samples to be continuously tested with increased temperatures and pressures than they would see in industry over long periods of time. For the first round of testing, a simple setup was used, where samples were taped directly to a cold stage at 5-10°C and steam produced from a cartridge heater immersed in a beaker of water. For secondary and final testing, a new setup was built to minimize contamination and extend the continuous length of tests. As seen in Figure 3-3, this design features a condensation chamber attached to a boiler and operates at 100°C and positive pressure.

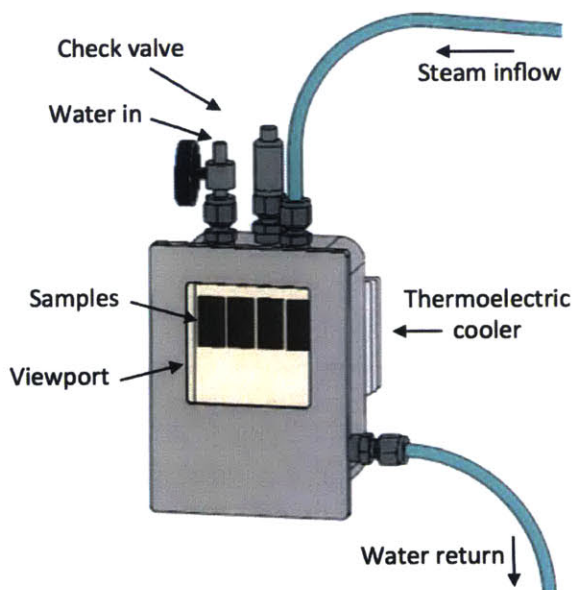


Figure 3-3: Schematic of accelerated condensation setup to determine effects of elevated temperatures and pressures for extended continuous condensing periods. Water return and steam inflow lines are connected to a boiler.

This setup has a boiler with rope heater set to 110°C and a clear 1/4" OD steam line connected to the top of the setup. Saturated steam at 100°C enters the condensation chamber, purging out air and non-condensable gasses. As the steam condenses, it collects in the bottom of the chamber and returns to the boiler through a flexible 1/2" OD tube, as seen in the schematic. Samples are mounted to double sided copper tape on foil, with a layer of kapton tape attaching the top and bottom of the sample to minimize a water layer forming between the samples and foil. The foil is then secured to the back of the chamber with vacuum tape and a metal clip screwed into the chamber wall. A one-way pressure valve is attached to the top of the chamber to vent steam when excess pressure builds up inside, without letting non-condensable gasses into the system. A water inlet valve is also mounted at the top of the chamber

to allow the addition of water as needed during testing. A thermoelectric stage is mounted to the back of the chamber and maintained at  $60^{\circ}\text{C}$  to provide a sample subcooling of around  $5^{\circ}\text{C}$ . This measurement was performed with a thermocouple welded to the inside of the condensation chamber during preliminary testing, and may have a slightly smaller subcooling for samples mounted to a foil sheet instead of directly to the wall. Since this setup amplifies the most challenging aspects of industrial use while combining the thermal and mechanical stresses of condensation, it gives a conservative estimate of expected sample robustness in an ACC. An image of the setup during testing is shown in Figure 3-4c.

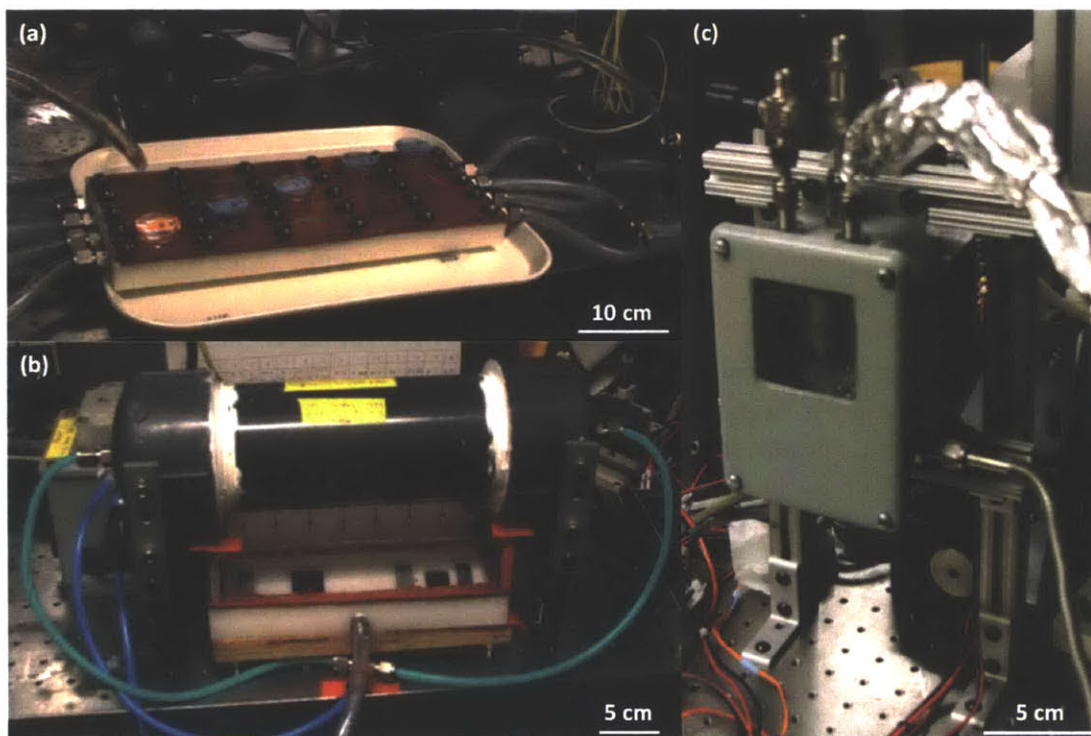


Figure 3-4: Images of flow setup (a), drop impingement setup (b), and accelerated condensation setup (c). Samples were tested over the course of two weeks with contact angle measurements taken periodically.

# Chapter 4

## Results of Robustness Testing

Samples were tested for durations of 3 days to 2 weeks, as detailed in section 4.1. The main characterization techniques, discussed in section 4.2, used were microgoniometer contact angle measurements, and scanning electron microscopy (SEM) imaging. Overall, the polymer coating from P2i generally remained intact, especially on CuO nanostructures on copper or stainless substrates. The CuO nanostructures showed very little change, but ZnO nanostructures generally had poor adhesion, especially for condensation tests. The ZnO adhesion was somewhat improved (though not eliminated) through the addition of an electroplated nickel layer. The silane and thiol coatings served for first round testing, but showed more degradation than the polymer coatings which were used exclusively for second and final round tests. Details of all of these results are presented in section 4.3.

### 4.1 Robustness Testing Rounds and Schedules

Three rounds of testing were done, with development and advancement of custom-built setups, to investigate nanostructure and coating robustness. For the first round of testing, accelerated condensation and drop impingement tests were run using simplified setups, with ZnO nanowires on silicon. This substrate was used because the extremely smooth, uniform surface bonds well to ZnO nanowires, and is easy to image. Coatings tested were polymer coatings from P2i and Semblant, stearic acid, and TFTS silane. Tests were run for 14 days straight before contact angle analysis and SEM imaging.

To investigate additional nanostructure and substrate combinations and better monitor degradation of structures and coatings, a second round of tests were performed. Second round samples were tested for up to 168 hours or until clearly wetting over the course of 12 days, to allow for drying time before imaging. Drying time was important in obtaining reliable measurements as measured contact angles on samples (especially the flooded condensation samples) were significantly lower due to the water film at the base of the nanostructures. After 168 hours of testing, samples with contact angles within 95% of initial angles were tested for an additional, continuous 168 hours. These tests used the setups detailed in the previous chapter, with periodic

sample removal and replacement after drying and measuring contact angles according to the schedule provided in table 4.1.

Table 4.1: Duration of robustness tests and dry times before measurements (hours).

Sample	Day:	1	2	3	6	7	10	11
Flow	Test (hr)	12	24	48	24	48	12	
	Dry (hr)	6	4	13	6	15	50	
Drop impingement	Test (hr)	12	24		48	24	48 <sup>1</sup>	12
	Dry (hr)	6	4	13	6	15	50	
Accelerated condensation	Test (hr)	12	20 <sup>2</sup>	48	4 <sup>2</sup>	48 <sup>1</sup>	12	24
	Dry (hr)	6	4	13	6	15	9	15

<sup>1</sup>Stainless steel samples were imaged during this test, drop impingement sample was then tested for 46 hours, and condensation sample was not tested

<sup>2</sup>Continuous Condensation setup required maintenance and tests were rescheduled

The second round of testing was aimed at tracking contact angles over the course of the tests, and was an acceptable method for continuous condensation and flow tests where exact sample placement is unnecessary. However, for the drop impingement setup, this allowed drops to impinge on slightly different areas on the samples (especially for ZnO samples on which the drop site was not visible). This issue was eliminated in the final round of tests which obtained contact angles before and after three days, one week, and two weeks of testing for different samples. There were also difficulties obtaining receding contact angles for the first two testing rounds as detailed in section 4.2, so final testing for the accelerated condensation and drop impingement setups used a custom contact angle setup described in section 4.2.1.

## 4.2 Robustness Characterization

Jumping condensation relies heavily on superhydrophobic surfaces with few defect sites. Therefore, the main characterization metrics are change in advancing and receding contact angles, and visual observations of nanostructure degradation. Advancing and receding contact angles are obtained with use of a micro-goniometer and image processing, to determine the angle between liquid and solid as the contact line of a drop moves on a surface. While advancing angles mainly provide a general idea of wetting properties of the surface bulk, degradation of the coating or nanostructures will present as defect sites which become apparent in receding angles. In this case the drop edge will become pinned on the more wetting defect site resulting in drop hysteresis, where the contact angle changes without movement of the base. If the defect or defects are small and surface tension can overcome the decreased surface energy of the substrate, the base will move again at a much lower contact angle. If the defect site or sites are too large and wetting, the drop will remain pinned and will instead only change contact angle hysteresis until evaporated. A complete con-

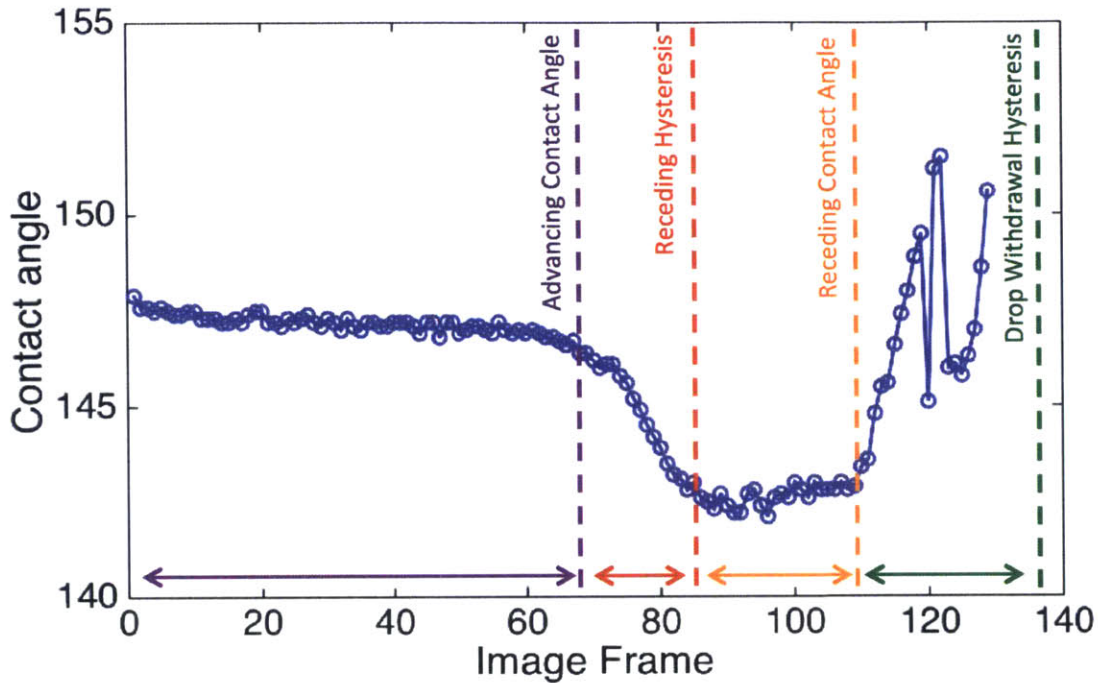


Figure 4-1: Evolution of contact angles for drop injection and withdrawal for CuO with polymer coating (P2i) after one week of drop impingement testing.

tact angle measurement is depicted in Figure 4-1 with hysteresis and base movement sections labeled.

Images were obtained through scanning electron microscopy (SEM). Coatings are difficult to characterize quantitatively with SEM due to their thickness (around 40nm), but structural damage or removal of nanostructures is easy to see and categorize as delamination or erosion. Since the coatings are expected to protect the samples from direct contact with water or steam, changes seen in these images will represent complete destruction of the sample. In these cases, the samples destroyed will not be candidates for industrial implementation.

These characterization methods are a good start in identifying failure mechanisms for nanostructures, but a more complete understanding of overall sample durability would be obtained through additional analysis focused on coating robustness. This might include chemical analysis through X-ray photoelectron spectroscopy (XPS) or Energy-dispersive X-ray spectroscopy (EDS), or focused ion beam (FIB) milling to allow for SEM imaging of a cross section.

#### 4.2.1 Contact Angle Measurement

Contact angles are frequently obtained with a commercially available micro-goniometer. For a typical setup, either a piezoelectric head or a glass needle with pump are used. In the case of a piezoelectric head, a tiny stream of droplets is injected towards the surface to form a coalesced drop for advancing angles, and evaporate for receding

angles. While this is an effective method for hydrophilic to moderately hydrophobic surfaces, on superhydrophobic samples the drops instead scatter on the surface until they find a pinning defect site to grow on. Not only does this make finding and focusing on individual drops extremely difficult, but base pinning frequently results in dramatic contact angle hysteresis instead of an advancing or receding base, as shown in Figure 4-2.

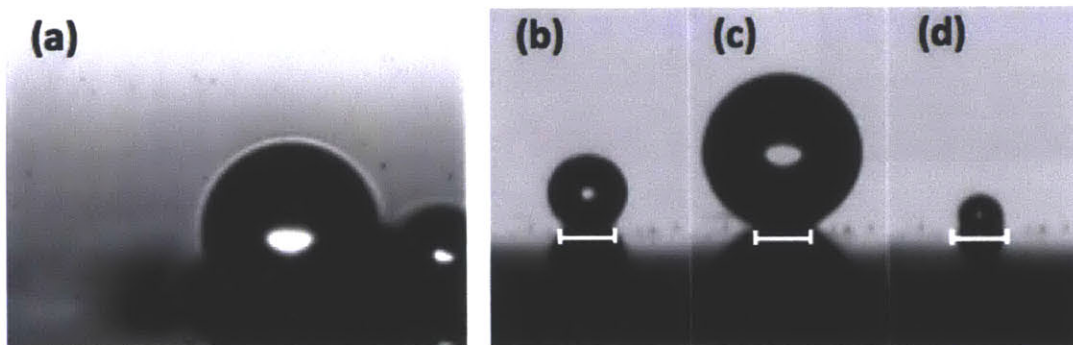


Figure 4-2: Example of typical scattering (a) using a micro-goniometer on a superhydrophobic surface. Once a drop pins on a defect site (b) the resulting drop growth (c) and evaporation (d) only results in contact angle hysteresis. The base diameter of drops and length of white bars ( $\approx 15\mu\text{m}$ ) in (b-d) are the same.

With a glass needle, a small drop is pumped out the end of the needle where it is pinned between the needle and surface. However at such small length scales, the surface energy of the glass is sufficiently higher than that of the surface, allowing drops to wick up the outside of the needle instead of contacting the surface. There are coatings that can be used to reduce the surface energy of the glass, minimizing this effect for hydrophobic surfaces, but even these coatings have sufficiently high surface energy to prove ineffective for measurements on superhydrophobic surfaces. Therefore, a custom setup was constructed and used to avoid these issues. A micro syringe pump (UltraMicroPump, World Precision Instruments) was used to deliver a fixed volume drop onto a height adjustable z-stage, as seen in in image 4-3. The advancing and receding angles were obtained by injecting (advancing) and withdrawing (receding) the liquid drop from the syringe pump. The drop was captured with a digital camera (EOS Rebel T2i, Canon), with initial tests relying on 2-5 advancing and receding contact angles (each) at 2-3 different locations. For second round testing, this was processed with the software ImageJ using the Dropsnake plugin. Final testing recorded a .mov file that was broken into frames and processed through FAMAS software. Analysis was done with the external setting which allows for angle fitting with a needle breaking the drop outline, and ellipse fitting method, as seen in Figure 4-4.

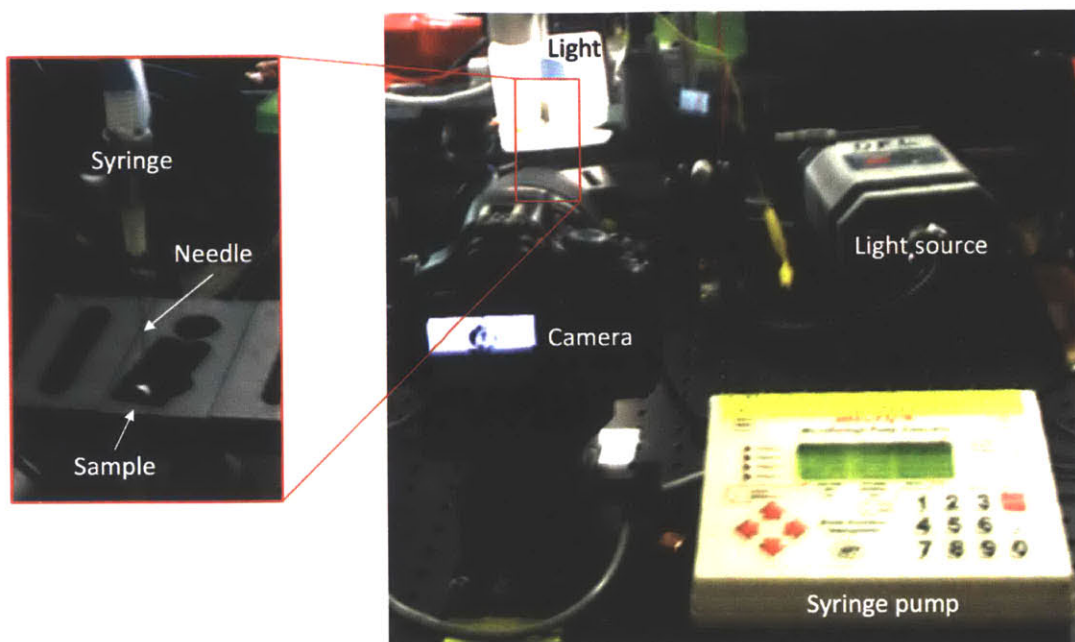


Figure 4-3: Custom micro-goniometer setup used to obtain contact angles. The camera images advancing and receding contact angles as a drop is injected onto the sample with the syringe pump and then pulled back.

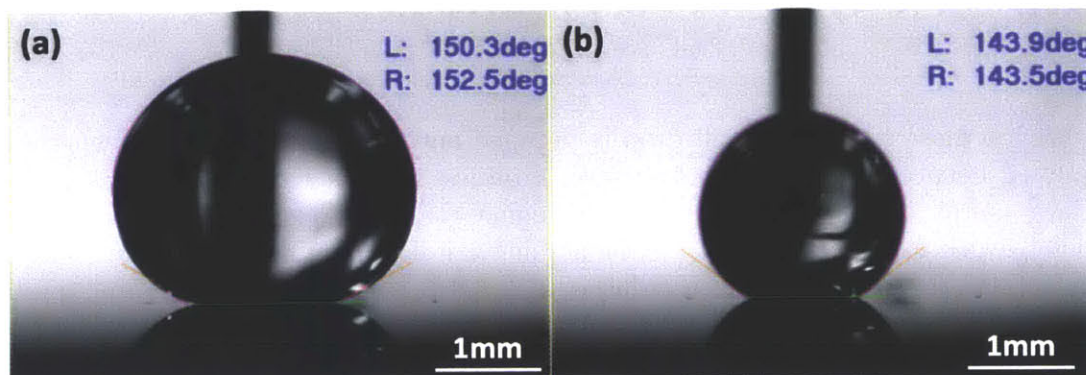


Figure 4-4: Images of the contact angle measurement using FAMAS software for (a) advancing and (b) receding contact angles after three days of accelerated condensation testing. The sample displayed has polymer coated (P2i) ZnO nanowires on a stainless steel substrate with a nickel adhesion layer. After the interface (green line) is drawn, the image processing splines (faint pink lines) measure the contact angle.

### 4.2.2 Error Analysis

All recorded contact angles (advancing, and when possible, receding) were the averaged advancing or receding value of 2-5 locations over the sample. This was done to provide an estimate of the uniformity of the surfaces, as many of the samples had varying performance depending on location. This was especially prevalent across the drop sites for drop impingement samples, indicating highly localized damage. It was also prevalent with most ZnO nanowire samples, due to inconsistent adhesion, possibly as a result of cleaning, seed layer distribution, or native surface passivation as discussed in section 2.1.2. Advancing and receding contact angles on each location were also not always constant, as defect sites result in contact angle hysteresis while the base is advancing or receding. In these cases, an average of the contact angles while the drop base radius was increasing or decreasing was used. Error bars reflect this inconsistency by taking into account the mean,  $\mu$ , standard deviation,  $\sigma$ , and number,  $n$ , of the locations characterized. They are calculated using 'Students t-distribution' 95% confidence intervals according to

$$errorbars = \mu \pm Z_{.95} * \frac{\sigma}{\sqrt{n}}, \quad (4.1)$$

where  $Z_{.95}$  values are tabulated based on % confidence interval and number of degrees of freedom ( $n$ ).

## 4.3 Robustness Characterization Results

Contact angles were obtained for all samples before and after testing. Results from the flow setup tests are provided in section 4.3.1, exhibit limited degradation. Results from the drop impingement tests and accelerated condensation tests are provided in sections 4.3.2 and 4.3.3, respectively, with relevant failure modes presented. For all plotted data, each data point is the averaged advancing or receding value over multiple different locations on the sample. Error bars are reported with 95% confidence, as discussed in section 4.2.2.

### 4.3.1 Flow Setup Robustness Results

The flow setup was intended to characterize resistance to mechanical stresses from flow, perpendicular to the coated nanostructures, at the high flow rates used in industrial steam condenser tubes. The advancing contact angles, taken with respect to the testing schedule in table 4.1 with SEM images of coated nanostructured surfaces are shown in Figure 4-5.

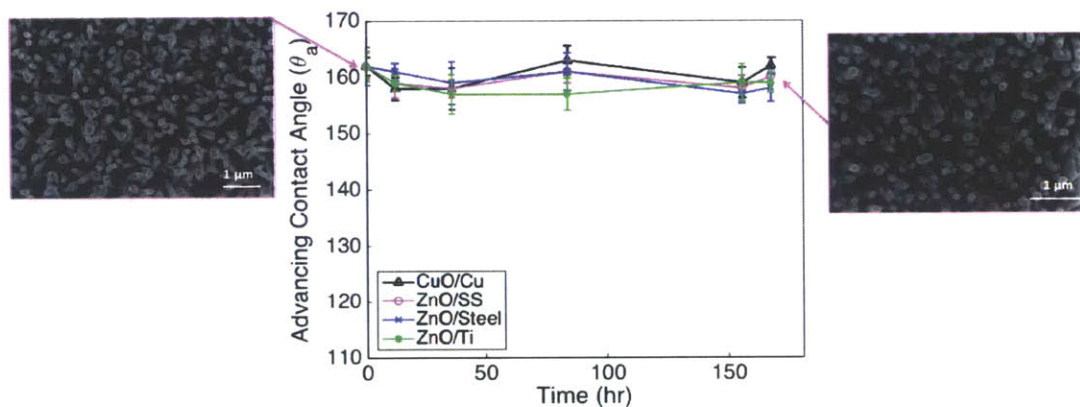


Figure 4-5: Flow setup advancing contact angle measurements over 1 week (168 hours). Each data point is the averaged value over multiple measurements on different locations on the sample. A polymer coating from P2i was used for all samples. Error bars represent 95% confidence intervals. SEM credits: B. Barabadi, D. Preston.

As is seen from Figure 4-5, contact angles over one week of testing show no change within calculated error. A protective air film was observed on the surface of the samples suggesting that durability of the hydrophobic coating is critical for surface longevity. Lack of failure mechanism, required setup maintenance, and shortage of samples, resulted in the postponement of further testing. While the lack of sample degradation is promising, one week of testing, especially with intact air film, is not sufficient to assume that the shear flows will not affect the samples. Therefore, additional testing is required, as suggested in section 6.2.

### 4.3.2 Drop Impingement Results

The drop impingement setup was designed to observe changes to coatings and nanostructures resulting from repeated localized drop impacts. Contact angle results from the first round of testing are provided in table 4.2.

Table 4.2: Contact angles for initial impingement testing.

Sample	Initial $\theta_a$ [ $^\circ$ ]	[ $\pm^\circ$ ]	Final $\theta_a$ [ $^\circ$ ]	[ $\pm^\circ$ ]
ZnO/Si polymer coating (P2i)	160	-	130	-
ZnO/Si stearic acid	157	1.6	88.5	2.7
ZnO/Si polymer coating (Semblant)	155	-	90	-

The results of this test suggest that the expected damage on samples was present. This was due to the extremely high water hammer pressures and shock wave propagation through the liquid upon impact. It also suggested that the polymer coating from P2i appeared to be most mechanically stable, which was used for all future testing.

Results of secondary and final round testing are consistent with preliminary findings, especially for ZnO nanostructures. The contact angle results from the second round with a total of 2 weeks (336 hours) of testing over the course of 19 days are displayed in Figure 4-6.

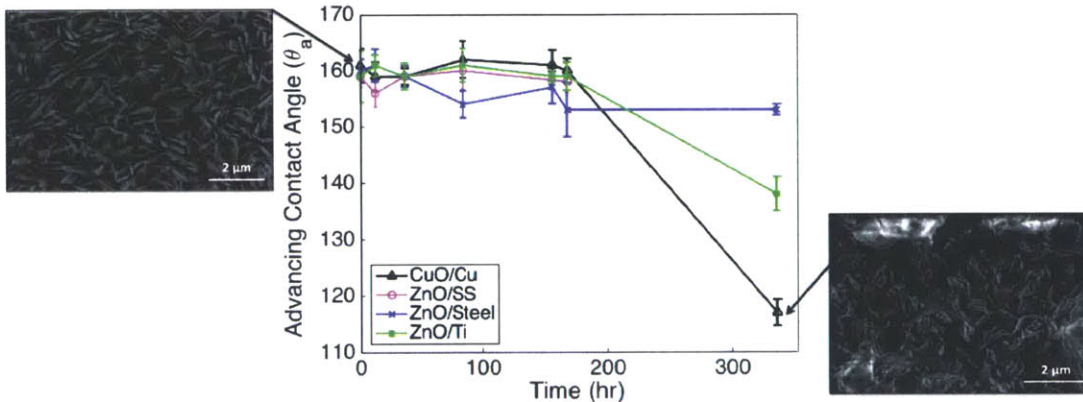


Figure 4-6: Second round drop impingement advancing contact angle measurements for 2 weeks (336 hours) of testing. A polymer coating from P2i was used for all samples. Error bars represent 95% confidence intervals. Left SEM credit: B. Barabadi.

The first week of testing shows little change within measurement error due to sample placement. After samples were removed for contact angle analysis, realignment in the setup afterwards was extremely difficult. Placement was better for the CuO sample, as the drop site was faintly visible on the otherwise uniform, flat black surface. Therefore, the final result for the CuO sample can be considered valid for a two week test, while the final results for the ZnO samples on titanium and low carbon steel are more indicative of one week of testing. Since the etched CuO nanoblades did not

appear significantly altered through SEM imaging, this round of testing demonstrate a coating degradation mode instead of only nanostructure delamination as seen in first round testing.

Alignment issues were eliminated for the final round of testing by only using samples for one time period. Two samples each of CuO on copper and ZnO on stainless with a nickel layer were used, and one sample each of ZnO directly on stainless steel, and CuO on stainless steel were used. All samples were again coated with a polymer coating (P2i). One of each sample was tested for 168 hours (one week), and duplicated samples were tested for 260 hours, at which point both showed indications of wetting. These results are depicted in Figure 4-7.

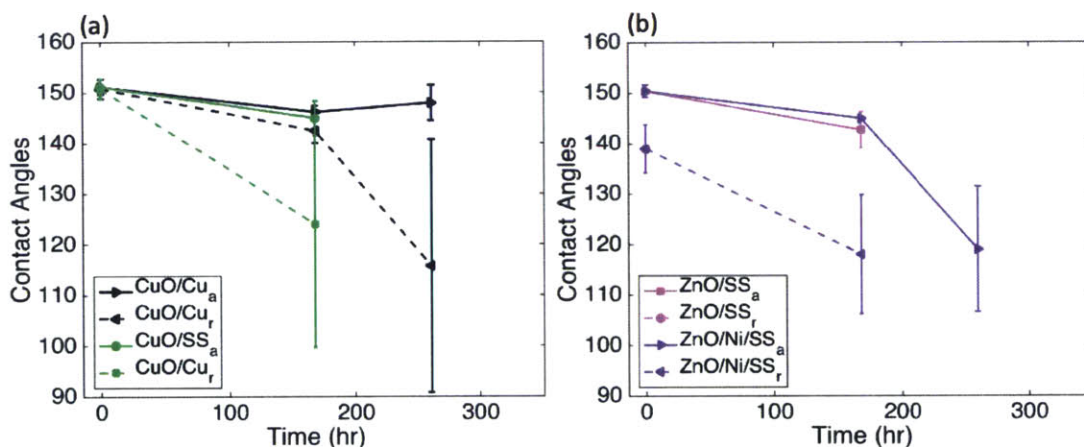


Figure 4-7: Final drop impingement testing round for CuO on copper and stainless steel (a), and ZnO on stainless steel with and without a nickel layer (b). Advancing (subscript a, solid line) and receding (subscript r, dashed line) contact angle measurement data. A polymer coating from P2i was used for all samples. Error bars represent 95% confidence intervals.

After one week of testing, the CuO samples were still completely repellent to the impinging drops. Contact angles for the CuO nanoblades etched into copper were constant within error. The advancing angle for CuO nanoblades etched into electroplated copper on stainless steel also remained constant within error, but receding angles were significantly lower. There was also significant variation for contact angle across the drop site, as reflected by large error bars, indicating that the damage site was extremely localized. After 260 hours of testing, a small wetting site was observed on the CuO on copper sample. This is consistent with the significantly deteriorated receding angle, and indicates the introduction of defect sites. SEM images of the CuO on stainless after 168 hours (Figure 4-8a), and CuO on copper after 260 hours (Figure 4-8b), do not display clear nanostructure degradation. This suggests that hydrophilic surface contamination is present, or that the water hammer pressure resulted in the removal of the polymer coating. These possibilities should be further analyzed as suggested in section 6.2.

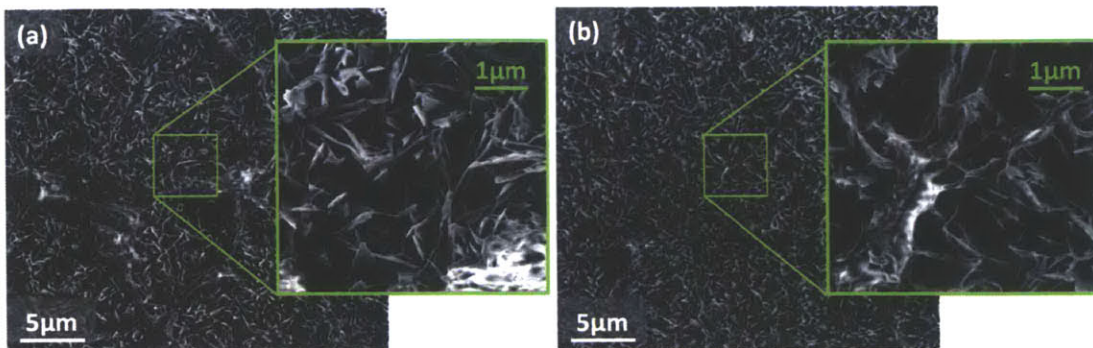


Figure 4-8: SEM images of polymer coated (P2i) CuO on stainless steel after 168 hours (a), and CuO on copper after 260 hours (b) of drop impingement testing.

Though the drop impingement site was clearly visible with unaided eye, it was not possible to find a specific defect site on the sample through SEM imaging. Therefore, samples were scored around the impact site to ensure that imaging locations could be as precise as possible.

In contrast, the sample with ZnO nanowires grown directly onto stainless steel was wetting after only one week of testing. Upon contact angle analysis, this sample had drop pinning to the extent that a receding contact angle could not be obtained. This is a result of nanostructure delamination in addition to potential coating degradation (as seen on the CuO samples) and was observed through SEM imaging in Figure 4-9.

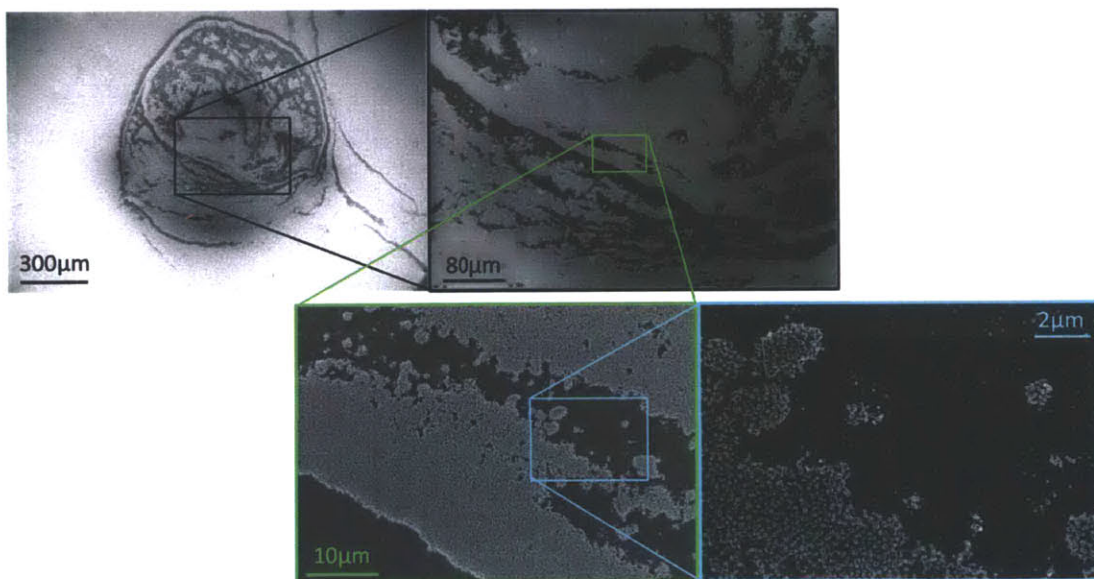


Figure 4-9: SEM images of ZnO on stainless steel after one week of drop impingement testing, demonstrating the only nanostructure degradation observed in this test setup.

The ZnO samples with additional nickel layer preserved nanowire adhesion, and performed similarly to the CuO sample on stainless steel after the first week. The second sample quickly became wetting, and after 260 hours did not have a receding contact angle. SEM imaging after the tests, however, did not exhibit sections of nanowire delamination as with the previous sample with an unobtainable receding angle. The nanostructure instead appears to be covered with contamination or a destroyed coating as demonstrated in a representative section of the impact site displayed in Figure 4-10.

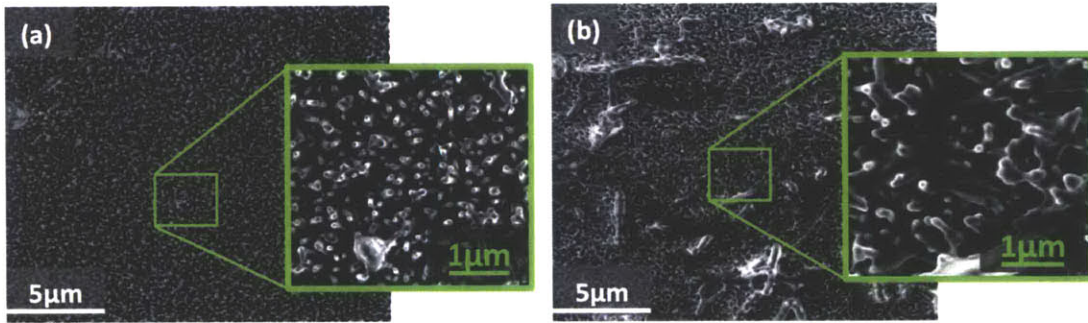


Figure 4-10: SEM images of ZnO on stainless steel with electroplated nickel after 168 hours (a) and after 260 hours (b) of drop impingement testing, both with a polymer coating from P2i.

This suggests that the bonding energy to the nickel adhesion layer is stronger than bonding energy to stainless steel. The lack of sample delamination also suggests that nanostructure shear stress is over 1.3 MPa. However, the low and then non-existent receding angles from degradation of coating or contamination must be addressed before this combination can be seriously considered for industrial implementation.

### 4.3.3 Accelerated Condensation Results

The final setup was designed to characterize sample resistance to thermal and mechanical stresses from a temperature gradient, and water wicking through the structures in a flooded condensation state. Three rounds of testing were performed with two different setups. The contact angle results from preliminary tests with ZnO on silicon are provided in table 4.3.

Table 4.3: Contact angles for initial condensation testing.

Sample	Initial $\theta_a$ [ $^\circ$ ]	[ $\pm$ ] $^\circ$	Final $\theta_a$ [ $^\circ$ ]	[ $\pm$ ] $^\circ$
ZnO/Si Polymer coating (P2i)	160	-	151	3.2
ZnO/Si stearic acid	157	1.6	142	2.9
ZnO/Si Polymer coating (Semblant)	155	-	133	69.5

All samples were observed to have small sections of nanowire delamination, as shown in Figure 4-14(b). The irregularities in contact angles for the same nanostructure/substrate combination suggest that the polymer coating from P2i is the most thermally stable.

Advancing contact angles for the second round of testing, which included ZnO on three metallic substrates (stainless steel, low carbon steel, and titanium) and a CuO sample, are shown in Figure 4-11.

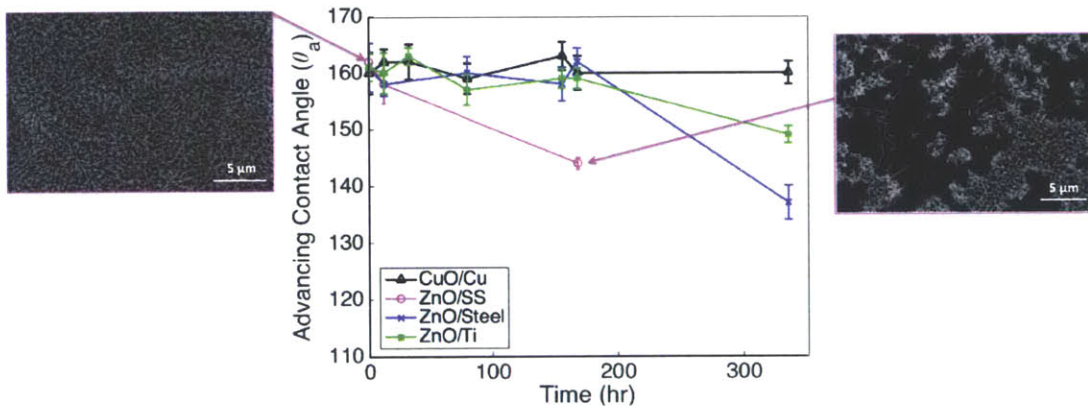


Figure 4-11: Advancing contact angle measurement data for accelerated condensation setup for a total of 2 weeks (336 hours) of testing over 19 days. A polymer coating from P2i was used for all samples. Error bars represent 95% confidence intervals. SEM image credits: D. Preston.

As can be seen by the dramatic decrease in advancing contact angles, the delamination which was observed on silicon substrates was exaggerated for the substrates used in second round testing, especially for stainless steel. The contrast between the stability of grown ZnO nanowires and etched CuO nanoblades after one week of testing is clear in Figure 4-14.

In an attempt to increase the adhesion between ZnO crystals and stainless steel, an electroplated nickel layer was added before nanowire growth for the final round of testing. A round of preliminary testing which compared ZnO on stainless with and without a nickel adhesion layer with a silane coating also demonstrated less delamination through visual SEM analysis. A sample with CuO nanoblades etched into electroplated copper and nickel on stainless steel was also added to determine stability of the electroplated layers, and investigate the potential of incorporating CuO nanoblades with other substrates. The results of these tests are seen in Figure 4-12.

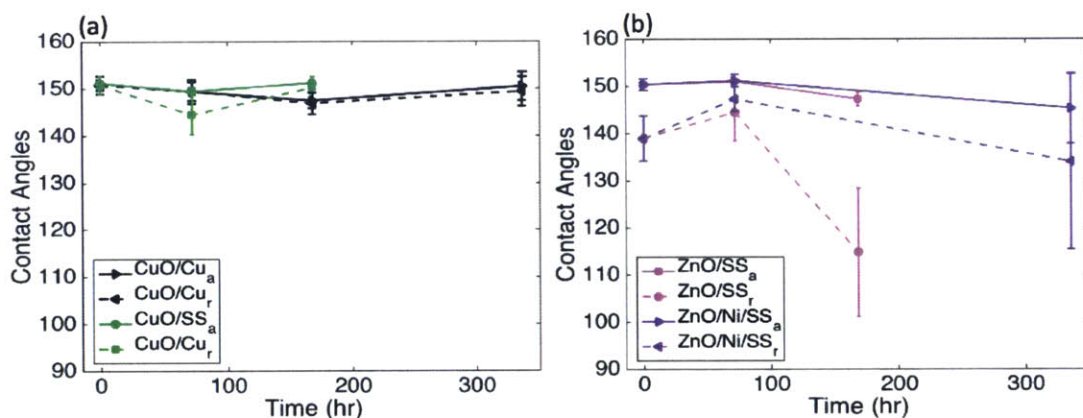


Figure 4-12: Final accelerated condensation testing round for CuO on copper and stainless steel (a), and ZnO on stainless steel with and without a nickel layer (b). Advancing (subscript a, solid line) and receding (subscript r, dashed line) contact angle measurement data. A polymer coating from P2i was used for all samples. Error bars represent 95% confidence intervals.

The CuO samples, both on copper and stainless steel substrates were unchanged within error for the durations of testing. This is consistent with all previous testing, and indicates that CuO nanoblades are viable candidates for industry. The durability of the CuO nanostructures on stainless steel is especially useful as it allows the possibility of superhydrophobic implementation with less expensive bulk materials, like low carbon steel.

The ZnO samples also proved to be consistent with previous tests, with delamination apparent on all samples, as seen in Figure 4-14. While the electroplated nickel adhesion layer appears to improve performance, the reduction in receding angle and visual delamination requires further testing and potential improvements before ZnO nanostructures should be considered for industrial implementation. An additional sample, with ZnO on stainless steel with nickel adhesion layer, had an uncharacteristically poor performance after one week of testing. As measurements for three days and two weeks were in visual agreement with the preliminary tests, and since ZnO growth is not consistent as suggested in section 2.1.2, this sample was omitted from the contact angle plot. All of these tests should also be repeated, since low water levels and very high boiler temperatures may have caused superheated steam to enter

the chamber. This, in combination with potentially poor thermal contact with the cold stage, may have resulted in significantly higher temperatures than anticipated for samples, which would exacerbate degradation due to thermal effects.

The tested samples also visually appear to have a significantly decreased coating thickness, as seen in Figure 4-13. Lack of a decreased receding contact angle measured for CuO samples, however, suggests that the functionality of the surface is not yet impaired. Further coating thickness characterization with focused ion beam milling is currently underway.

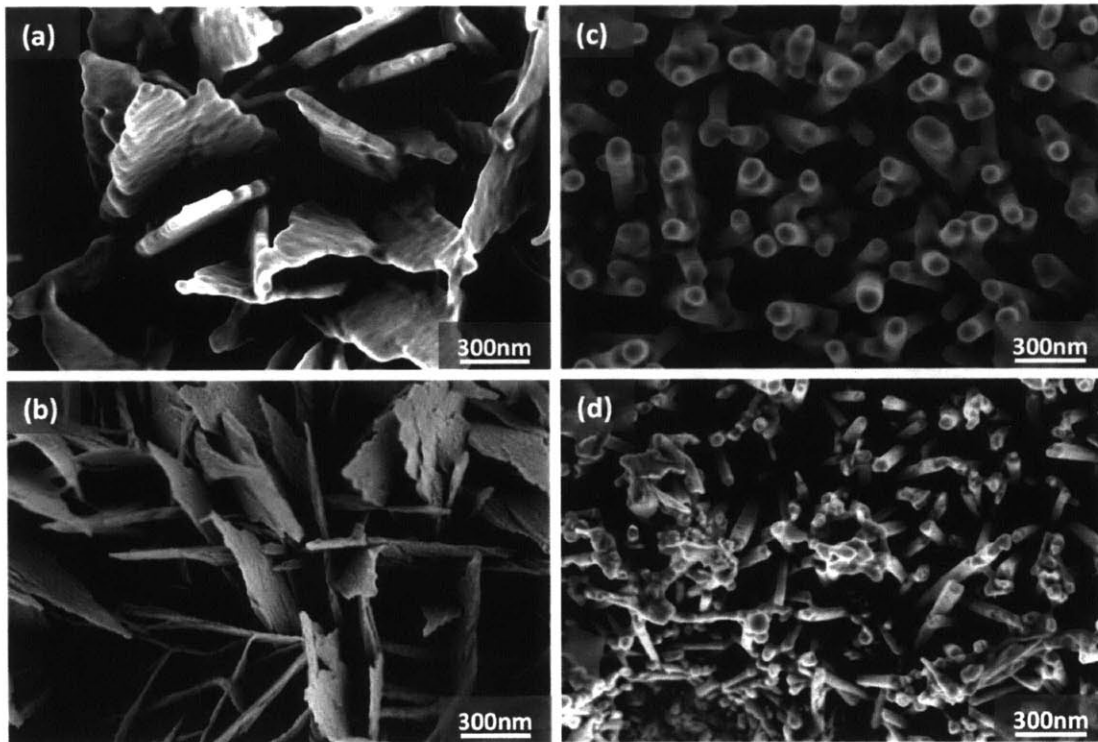


Figure 4-13: SEM images before (a,c) and after (b,d) two weeks of accelerated condensation testing for CuO on Copper (a,b) and ZnO on stainless steel with nickel layer (c,d), all with polymer coating (P2i).

The bulk in all ZnO images in Figure 4-14 are covered by nanowires, with holes exposing the substrates beneath. This suggests poor adhesion between the ZnO nanowires and substrates. In all cases except for the CuO sample, the image selected is representative of the bulk of the sample. Therefore, the best or worse sections are not displayed, which for titanium, steel, nickel, and stainless substrates vary from completely barren patches to completely preserved areas.

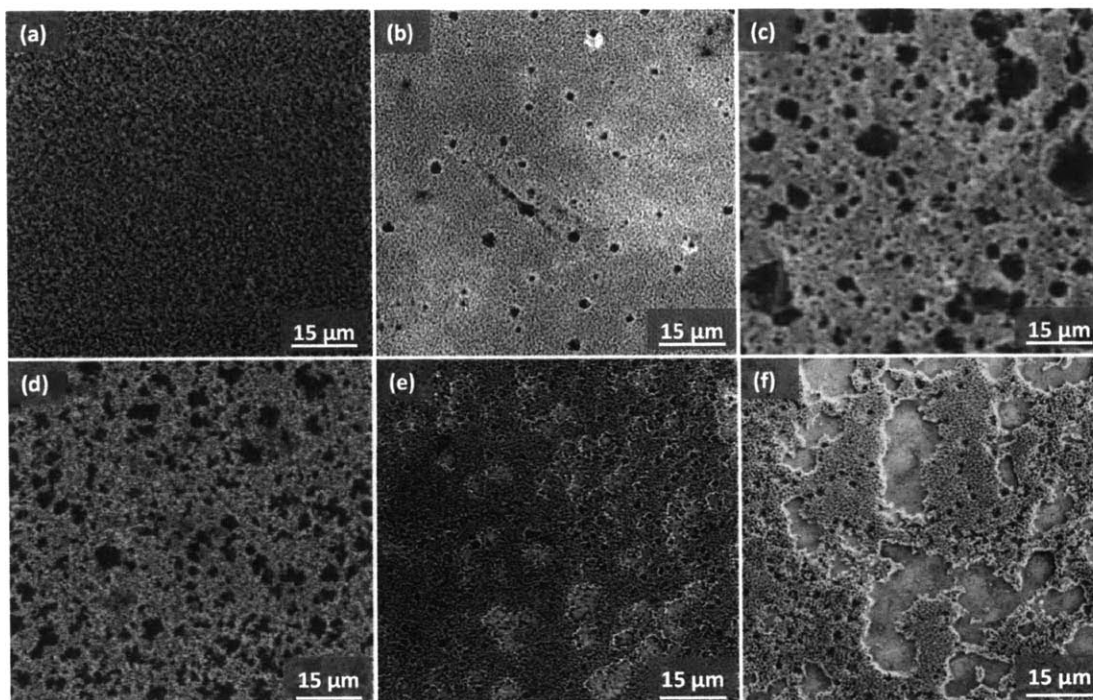


Figure 4-14: Representative SEM images of polymer coated (P2i) CuO nanoblades on copper (a) and ZnO nanowires on: silicon (b), titanium (c), low carbon steel (d), electroplated nickel (e), and stainless steel (f), after accelerated condensation testing. CuO on copper and ZnO on silicon and on stainless steel with nickel are imaged after two weeks of testing, the rest are imaged after one week of testing. SEM credit (c) and (d): B. Barabadi.

It is proposed that large mismatch in coefficient of thermal expansion (CTE) may be a significant factor determining durability. Commonly obtained CTE's are displayed in table 4.4, and a qualitative evaluation of surfaces from SEM images like those provided in Figure 4-14, indicate better adhesion for substrates with CTE most similar to that of ZnO nanowires. Consistent with this assessment, excellent adhesion between the stainless, electroplated nickel and electroplated copper layers has been observed. For the ZnO samples on nickel, SEM imaging reveals that the nickel layer, while rough, remains intact after nanostructure delamination.

Table 4.4: Coefficients of thermal expansion for relevant materials.

Material	$CTE \times 10^{-6} \frac{m}{m^{\circ}C}$
Silicon	3
ZnO	4
Titanium	8.6
410SS	9.9
Steel	12
Nickel	13
316SS	16
Copper	16.6

Titanium and 316 stainless steel surfaces perform worse than would be expected purely from CTE mismatch. These materials are known to be highly resistant to corrosion, with passivating natural oxide layers that limit adhesion in the absence of extremely acidic activating solutions. Therefore, surface bonding is also an important factor for consideration.

## 4.4 Robustness Conclusions

Over the course of robustness testing, etched CuO nanoblades demonstrated excellent durability, while grown ZnO nanowires had partial delamination on all substrates. The polymer coating from P2i showed good thermal and mechanical stability, but decreased contact angles for all drop impingement tests, and an observed thinning during accelerated condensation testing, suggests that additional testing is necessary.

In this chapter, three rounds of testing was done. The first round served to select a suitable coating, and identify any potential failure mechanisms. The two failure mechanisms identified, ZnO nanowire delamination and coating destruction, were persistent throughout all rounds of testing.

The second round test setups were then developed to monitor samples in more controlled environments, and a much wider variety of nanostructure and substrate combinations were tested. The initial failure mechanisms were again observed, and steps were taken to minimize ZnO nanowire delamination by adding an electroplated nickel adhesion layer. Based on the excellent performance of CuO nanoblades, steps were also taken to integrate CuO nanoblades with a stainless steel substrate. Test procedure shortcomings, mainly for the drop impingement setup, were identified and improved upon for final round testing.

The final round of testing demonstrated good performance from CuO nanoblades, both on copper and on stainless steel, and an improvement in adhesion between ZnO nanowires and stainless with the added electroplated nickel layer. Overall substrate, nanostructure, and coating performance and recommendations are provided in table 4.5.

Table 4.5: Investigated substrate, nanostructure, and coating combinations, and general performance. Materials are copper (Cu), 316 stainless steel (SS), nickel (Ni), carbon steel (CS), titanium (Ti), and silicon (Si).

Substrate	Nanostructure	Coating	Overall Performance
Cu	CuO	P2i	Good: consider for scaled-up testing
SS/Ni/Cu	CuO	P2i	Good: consider for scaled-up testing
SS/Ni	ZnO	P2i	Fair: continue testing and development
CS	ZnO	P2i	Fair: continue testing and development
Ti	ZnO	P2i	Fair: continue testing and development
SS	ZnO	P2i	Poor: develop before consideration
Si	ZnO	P2i	Fair: not applicable to industry
Si	ZnO	Semblant	Poor: not applicable to industry
Si	ZnO	stearic acid	Poor: not applicable to industry



# Chapter 5

## Closed Loop Internal Condensation Setup

A critical aspect of determining feasibility of implementing jumping condensation in industrial Air Cooled Condensers (ACC) is quantifying the improved heat transfer over existing technologies. It is also important to prove robustness of the superhydrophobic nanostructured surfaces in anisimilar geometry. Therefore, a dedicated closed loop internal condensation setup was designed with a boiler, test section, chiller, and required sensors to run tests and obtain data. In this chapter, setup requirements are summarized in section 5.1, and component details and selections are provided in section 5.2. A Schematic and CAD rendering of the setup is shown in Figure 5-1

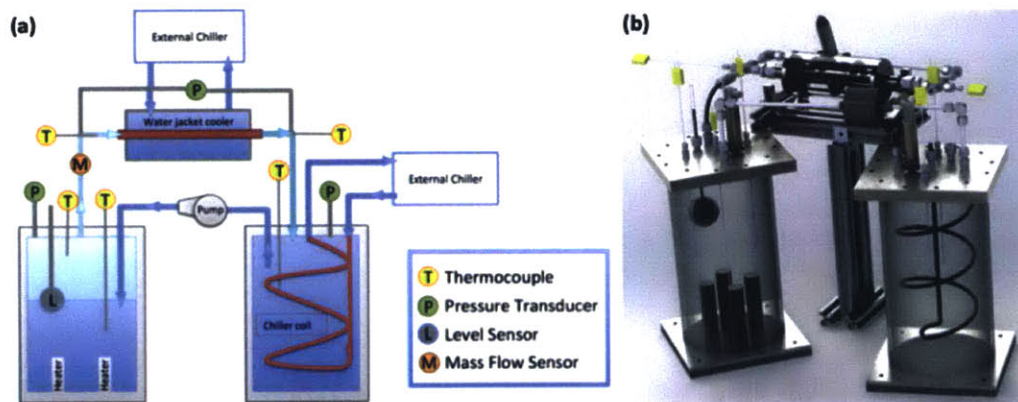


Figure 5-1: Schematic (a) and CAD render (b) of closed loop internal condensation setup.

### 5.1 Design Criterion

As introduced in chapter 1, jumping droplet condensation, has up to a 30% increase in heat transfer over dropwise condensation [26]. Another important metric of evaluating performance however, is the pressure drop across the test section. Jumping

condensation offers higher droplet removal and smaller droplets than filmwise or dropwise condensation, which may reduce this pressure drop. As very little work has been done to model jumping droplet condensation in internal flows, a laboratory scale setup is built to determine it experimentally. It was not practical to maintain an industrial aspect ratio for test sections, so the system was designed to match or exceed industry Reynolds numbers. By non-dimensionalizing pressure drop with the Euler number (5.1), it is possible to get appropriate scaling for pressure drop with respect to geometry.

The Euler number is defined as

$$Eu = \frac{\Delta P}{\left(\frac{\dot{m}^2}{A_c^2 \rho}\right)}, \quad (5.1)$$

where  $\Delta P$  is the pressure drop across the test section,  $\dot{m}$  is the mass flow rate of steam,  $A_c$  is the cross-sectional area of the test section, and  $\rho$  is the density of steam. It was also important to ensure that tests may be run continuously for extended periods of time, motivating the use of a closed loop setup.

## 5.2 Mechanical System Components

The main components of this closed-loop internal condensation setup are a boiler, test section with external cooling, chiller, and temperature, pressure, and level sensors. Each of these components and the motivation for their selection is described below.

### 5.2.1 Boiler and Reservoir

A 5L boiler produces saturated steam to be delivered to the test section with four 1000W Chromalox cartridge heaters. The boiler is made out of a 12 tall, 6 ID 304 stainless steel pipe section with welded base and top flange. A removable lid with attachments for sensors and fluid inlet/outlet (steam out and water in) is connected to the top flange with a series of bolts and an o-ring. The temperature of the boiler is controlled with a PID control loop to ensure dry but not superheated steam. The reservoir has similar dimensions and sensors as the boiler. The reservoir also contains a chiller/heat exchanger coil (connected to an external chiller) which will ensure complete condensation of the vapor before it is pumped back to the boiler. The use of a pump (magnetic gear pump GA-X21-DEMSE, Micropump) will ensure that the system is a closed loop and enable continuous operation.

### 5.2.2 Test Section

The test section tube, which connects the boiler and chiller, and is made from the desired combination of substrate, nanostructure, and hydrophobic coating as discussed in chapter 2. Currently 0.5 OD tubing is used due to easy implementation with the rest of the setup, and with justification described in section 5.1. However, any geometry can be interchanged, as long as sufficient external cooling is provided. With

laboratory space constraints, it is much more practical to substitute a direct water cooler for the air-cooling fan. This also allows greater control, which will aid in repeatable heat transfer measurements. The test section and cooler can be oriented at any angle.

### 5.2.3 Chiller

An external refrigerated chiller will be used to condense the steam in the test section and the reservoir. The chiller (ThermoScientific) is a recirculating bath chiller capable of temperatures from around 5°C to above ambient, around 150°C. This will allow a range of operating conditions to be tested, including accelerated testing at elevated temperatures.

### 5.2.4 Sensors

A variety of temperature, pressure, and mass flow sensors are required for monitoring operation and measuring heat transfer.

For the measurement of the steam flow through the test section, two main criteria need to be satisfied: (a) high temperature operation ( 50°C), and (b) low pressure drop (to prevent condensation). Experiments will be run in a vacuum, minimizing the required temperature range needed. The most extreme temperatures expected are 5°C for the chiller, and 70°C for the boiler. However, the system is capable of operating at higher temperatures for accelerated testing under adverse conditions. These requirements are met with type J thermocouple probes (Omega). As with the rest of the system, a stainless steel probe sheath is used to eliminate sensor corrosion or system contamination.

Two types of pressure sensors are required; one across the test section, and another for the boiler as part of the control loop to maintain stable operating conditions. A custom differential wet/wet unidirectional pressure transducer (0-5 psia Omega) was selected for test section, and high accuracy absolute pressure transducers (0 30 psia, Omega) were selected for the boiler and chiller.

Finally, to fully automate the system, another control loop is required to activate the pump between the boiler and reservoir to prevent the boiler from running dry. Most commercial level sensors are too large and expensive for this application, so two simple solutions are being investigated. One is a force pad or scale to activate the pump from chiller to boiler once the boiler mass is below a certain point. Another solution is to use a simple float with optical switch was created. Two light sensors are placed vertically in the range of the top of the float, with the pump being activated with the lower sensor is triggered due to the float being too low in the tank. Once the water level is adequate, the float rises and blocks the second light sensor, turning the pump off.

### **5.3 Closed Loop Internal Condensation Setup: Next Steps**

The closed loop internal condensation setup is currently in the process of being built, and will allow for the first characterizations of heat transfer measurements for internal jumping condensation. It is expected that the heat transfer for internal jumping condensation will be even higher than that for external jumping condensation, as droplet removal will be aided by shear forces in the steam flow. This setup will also serve as a preliminary version of scaled up testing, and can monitor the durability of surfaces through continuous heat transfer measurements over extended periods of time in an extremely controlled environment. Once substrate, nanostructure, coating combinations are proved successful in this setup over time, the expense of initiating fabrication and testing of much larger test sections can be justified.

# Chapter 6

## Conclusions and Future Work

### 6.1 Summary of Work

This work is the first step in quantifying the robustness of superhydrophobic nanostructured surfaces capable of inducing jumping droplet condensation in steam condensers. A variety of nanostructures, substrates, and coatings were investigated for thermal and mechanical durability. The durability of these surfaces was tested with industrially relevant, custom-built setups. These setups were designed to provide extended, continuous testing in controlled environments for observation of failure mechanisms. The first setup was designed to match the transition regime Reynolds number of steam flow in a scaled down laboratory setup to observe effects of shear stresses on the nanostructures and hydrophobic coating. The second setup was intended to simulate severe mechanical stresses from impinging drops that might coalesce or form on the top of the steam tube, and fall under gravity. The final setup was an accelerated condensation setup, designed to characterize thermal and mechanical stability at elevated temperatures and pressures.

The results after three sets of tests, lasting from three days to two weeks, indicate that CuO nanoblades, either on a copper substrate or etched into electroplated copper, are excellent candidates for scaled up testing. While this work only investigated copper electroplated onto type 316 stainless steel, the excellent adhesion suggests that it would also perform well on other substrates. Stainless steel is known for corrosion resistance, and is therefore considered difficult to plate, so success on this substrate is extremely promising for other materials.

The results of testing on ZnO nanowires is less definitive, as delamination was observed on all samples that experienced thermal stresses. The performance appears to be improved through use of an electroplated nickel adhesion layer. A significant mismatch in coefficient of thermal expansion between all metallic surfaces and zinc oxide crystals, however, indicates the need for further investigation. It is important to note that setup conditions were not ideal, so future tests should more carefully monitor sample temperature. While elevated temperatures are useful to assess degradation over time, conditions with super-heated steam will no longer be relevant for industrial applications.

Finally, three coatings (stearic acid, and fluorinated polymer coatings from Semblant and P2i) were tested in preliminary testing. In both drop impingement testing and condensation tests, the polymer coating from Semblant demonstrated the most degradation in contact angle, stearic acid demonstrated moderate degradation, and the polymer coating from P2i demonstrated the most durability. For second and final round testing, the polymer coating from P2i demonstrated good preservation in contact angle on intact nanostructures over the tests. A visual thinning of the coating, however, imaged through use of SEM and FIB milling, is concerning and will need to be monitored over longer periods of testing.

## 6.2 Future and Ongoing Work

This thesis aimed to develop methods of determining and characterizing the robustness of superhydrophobic nanostructured surfaces capable of inducing jumping-droplet condensation. While a start was made in characterizing performance and identifying failure mechanisms, more work should be done to identify additional potential surfaces, develop the surfaces currently under investigation, and analyze coating robustness.

This work investigated nanostructures and coatings already known for good jumping condensation performance, but there are many more alternative nanostructures and coatings possible. One of these nanostructures, etched TiO<sub>2</sub> nanowires, has shown promising robustness in preliminary testing. TiO<sub>2</sub> is especially appealing, because it is expected to exhibit similar durability to CuO nanoblades due to the etched fabrication method. It is also extremely relevant to ACC use as titanium is resistant to corrosion, and is considered a viable substrate for industrial use.

For future work with ZnO nanostructures, stainless steel type 410 should be also considered. While it may still have poor performance due to limited adhesion, it has a CTE of  $9.9 \times 10^{-6}$  m/m°C, which reduces the CTE mismatch between ZnO nanowires and substrate from  $12 \times 10^{-6}$  m/m°C for stainless steel type 316, to  $5.9 \times 10^{-6}$  m/m°C. Stainless steel type 410 also has a lower chromium content which may result in a less passive surface. It may also be possible to add a surface activation step alternative to nickel electroplating for improved adhesion.

Additional flow tests should combine a condensing surface, pre-flooded samples, or degassed water with the flow setup concept to determine degradation effects without the air film. In addition, longer term testing should be done with all of the setups, with more carefully monitored conditions. Also, additional characterization should be done to determine the chemical composition of the contaminants observed on the surface on all drop impingement samples. This measurement could be made with X-ray photoelectron spectroscopy (XPS) or Energy-dispersive X-ray spectroscopy (EDS), and would determine whether the bulk is from the coating, or external sources. If the latter, all surfaces except ZnO directly on stainless should be considered for scaled up testing.

Though results of external condensation demonstrate enhanced heat transfer for jumping condensation, this has not yet been shown for internal condensation. This

motivated the design and construction of the closed loop setup, which is ready to begin testing. This will hopefully aid in the development of modeling jumping drops in the internal steam flow, and provide confirmation of enhanced heat transfer. Once this has been completed, scaled up testing for longer periods of time should be performed. These tests will be able to more accurately simulate expected wear using more realistic geometries and conditions than possible in a laboratory environment.

Finally, an unexpected result was observed for smooth copper samples coated with the polymer coating from P2i. Both samples used (in two separate tests) demonstrated a significant *increase* in contact angle, from around  $136^\circ$ , to over  $155^\circ$ . The initial contact angle was somewhat higher than expected for a flat sample, but upon SEM imaging, globules of coating were observed, as seen in Figure 6-1b. After testing, parts of the sample had darkened from the initial bright copper color, to a faint green-black, and upon SEM imaging, it appeared that an oxide had formed on the surface during testing, as shown in Figure 6-1c.

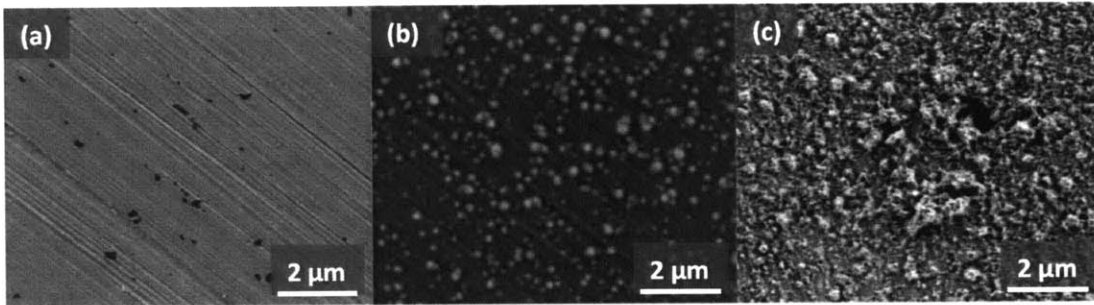


Figure 6-1: SEM images of a bare copper substrate (a), after coating with a polymer coating from P2i (b), and after 168 hours of accelerated condensation testing (c).

Future work should investigate the composition of these nanostructures, whether they are candidates for jumping condensation, and how robust they are over time. Regardless, the possibility of improving steam condenser performance during operation, by increasing the hydrophobicity through naturally occurring oxidation, is be very exciting.



# Bibliography

- [1] EIA, “March 2015 monthly energy review,” tech. rep., 2015.
- [2] K. F. Layton and D. G. Daniels, “Interim guidance - amine treatments in fossil power plants,” tech. rep., 2010.
- [3] Q. Zhao and B. Burnside, “Dropwise condensation of steam on ion implanted condenser surfaces,” *Heat Recovery Systems*, vol. 14, no. 5, pp. 525–534, 1994.
- [4] A. Mills and V. Ganesan, *Heat Transfer*. Prentice Hall, 2nd ed., 1999.
- [5] K. Wilber and J. Maulbetsch, “Air-cooled condenser design, specification, and operation guidelines,” tech. rep., 2005.
- [6] J. W. Rose, “Dropwise condensation theory and experiment: A review,” *Proceedings of the Institution of Mechanical Engineers, Part A: Journal of Power and Energy*, vol. 216, pp. 115–128, 1 2002.
- [7] A. Bisetto, D. Torresin, M. K. Tiwari, D. Del Col, and D. Poulikakos, “Dropwise condensation on superhydrophobic nanostructured surfaces: Literature review and experimental analysis,” *Journal of Physics: Conference Series*, vol. 501, 4 2014.
- [8] T. Young, “An essay on the cohesion of fluids,” *Philosophical Transactions of the Royal Society of London*, vol. 95, pp. 65–87, 1805.
- [9] P.-G. de Gennes, F. Brochard-Wyart, and D. Quere, *Capillarity and Wetting Phenomena Drops, Bubbles, Pearls, Waves*. Springer, english tr ed., 2004.
- [10] D. Quéré, “Wetting and roughness,” *Annual Review of Materials Research*, vol. 38, pp. 71–99, 8 2008.
- [11] R. N. Wenzel, “Resistance of solid surfaces to wetting by water.,” *Journal of Industrial and Engineering Chemistry (Washington, D. C.)*, vol. 28, pp. 988–994, 1936.
- [12] A. B. D. Cassie and S. Baxter, “Wettability of porous surfaces,” tech. rep., 1944.
- [13] A. Chandekar, S. K. Sengupta, and J. E. Whitten, “Thermal stability of thiol and silane monolayers: A comparative study,” *Applied Surface Science*, vol. 256, pp. 2742–2749, 2 2010.

- [14] M. Lee, G. Kwak, and K. Yong, "Wettability control of zno nanoparticles for universal applications," *ACS Applied Materials and Interfaces*, vol. 3, no. 9, pp. 3350–3356, 2011.
- [15] A. Ulman, "Formation and structure of self-assembled monolayers," *Chemical reviews*, vol. 96, pp. 1533–1554, 6 1996.
- [16] Y. Wang, B. Li, T. Liu, C. Xu, and Z. Ge, "Controllable fabrication of superhydrophobic tio<sub>2</sub> coating with improved transparency and thermostability," *Colloids and Surfaces A: Physicochemical and Engineering Aspects*, vol. 441, pp. 298–305, 2014.
- [17] T. Wu, Y. Pan, and L. Li, "Study on superhydrophobic hybrids fabricated from multiwalled carbon nanotubes and stearic acid," *Journal of Colloid and Interface Science*, vol. 348, no. 1, pp. 265–270, 2010.
- [18] M. M. Derby, A. Chatterjee, Y. Peles, and M. K. Jensen, "Flow condensation heat transfer enhancement in a mini-channel with hydrophobic and hydrophilic patterns," *International Journal of Heat and Mass Transfer*, vol. 68, pp. 151–160, 1 2014.
- [19] D. Torresin, M. K. Tiwari, D. Del Col, and D. Poulikakos, "Flow condensation on copper-based nanotextured superhydrophobic surfaces," *Langmuir : the ACS journal of surfaces and colloids*, vol. 29, pp. 840–8, 1 2013.
- [20] D. Quéré, "Non-sticking drops," *Reports on Progress in Physics*, vol. 68, pp. 2495–2532, 11 2005.
- [21] S. Kumagai, S. Tanaka, H. Katsuda, and R. Shimada, "On the enhancement of filmwise condensation heat transfer by means of the coexistence with dropwise condensation sections," *Experimental Heat Transfer*, vol. 4, pp. 71–82, 1 1991.
- [22] J. B. Boreyko and C.-H. Chen, "Self-propelled dropwise condensate on superhydrophobic surfaces," *Physical Review Letters*, vol. 103, no. 18, 2009.
- [23] N. Miljkovic and E. N. Wang, "Condensation heat transfer on superhydrophobic surfaces," *MRS Bulletin*, vol. 38, pp. 397–406, 5 2013.
- [24] N. Miljkovic, *Development and Characterization of Micro / Nanostructured Surfaces for Enhanced Condensation*. PhD thesis, 2013.
- [25] D. J. Preston, *Electrostatic Charging of Jumping Droplets on Superhydrophobic Nanostructured Surfaces : Fundamental Study and Applications*. PhD thesis, 2014.
- [26] N. Miljkovic, R. Enright, Y. Nam, K. Lopez, N. Dou, J. Sack, and E. N. Wang, "Jumping-droplet-enhanced condensation on scalable superhydrophobic nanostructured surfaces," *Nano letters*, vol. 13, pp. 179–87, 1 2013.

- [27] N. Miljkovic, R. Enright, and E. N. Wang, "Modeling and optimization of superhydrophobic condensation," *Journal of Heat Transfer*, 2013.
- [28] A. Lafuma and D. Quere, "Superhydrophobic states," *Nature materials*, vol. 2, 2003.
- [29] R. Enright, N. Miljkovic, A. Al-Obeidi, C. V. Thompson, and E. N. Wang, "Condensation on superhydrophobic surfaces: the role of local energy barriers and structure length scale.," *Langmuir : the ACS journal of surfaces and colloids*, vol. 28, pp. 14424–32, 10 2012.
- [30] J. Maulbetsch, "Nsf-epri workshop," in *ASME-IMECE*, ASME-IMECE, 2012.
- [31] J. L. Tsou, J. Maulbetsch, and J. Shi, "Power plant cooling system overview for researchers and technology developers," tech. rep., 2013.
- [32] J. Maulbetsch, "Economic evaluation of alternative cooling technologies," tech. rep., 2011.
- [33] M. W. Larinoff, W. E. Moles, and R. Reichhelm, "Design and specification of air-cooled steam condensers.," *Chemical Engineering (New York)*, vol. 85, no. 12, pp. 86–94, 1978.
- [34] HEI, "Standards for air cooled condensers," tech. rep., 2011.
- [35] J.-P. Libert and D. Zhaovi, "Air cooled steam condenser test laboratory," in *Cooling Tower Technology Conference*, 2012.
- [36] C. Brinker and G. Scherer, eds., *Sol-Gel Science, The Physics and Chemistry of Sol-Gel Processing*, vol. 3. Academic Press, 1991.
- [37] A. C. Pierre, *Introduction to Sol-Gel Processing*. Springer, 1998.
- [38] R. Sui and P. Charpentier, "Synthesis of metal oxide nanostructures by direct sol gel chemistry in supercritical fluids," *Chemical Reviews*, vol. 112, pp. 3057–3082, 2012.
- [39] A. C. Pierre and G. M. Pajonk, "Chemistry of aerogels and their applications," *Chemical reviews*, vol. 102, pp. 4243–65, 12 2002.
- [40] H. Tamon and H. Ishizaka, "Influence of gelation temperature and catalysts on the mesoporous structure of resorcinol-formaldehyde aerogels," *Journal of colloid and interface science*, vol. 223, pp. 305–307, 3 2000.
- [41] S. Xu and Z. L. Wang, "One-dimensional zno nanostructures: Solution growth and functional properties," *Nano Research*, vol. 4, pp. 1013–1098, 8 2011.
- [42] R. Narhe, W. González-Viñas, and D. Beysens, "Water condensation on zinc surfaces treated by chemical bath deposition," *Applied Surface Science*, vol. 256, pp. 4930–4933, 6 2010.

- [43] J. Hajdu, “Surface preparation for electroless nickel plating,” *Electroless Plating*, pp. 193–206.
- [44] P. H. Baner, “Why passivate stainless steel and what happens if you dont,” tech. rep., 2008.
- [45] TechnicInc, “Woods nickel strike,” tech. rep., 2000.
- [46] G. Gu, B. Zheng, W. Q. Han, S. Roth, and J. Liu, “Tungsten oxide nanowires on tungsten substrates,” *Nano letters*, vol. 2, no. 8, pp. 849–851, 2002.
- [47] W. Lee, B. G. Park, D. H. Kim, D. J. Ahn, Y. Park, H. Lee, and K. B. Lee, “Nanostructure-dependent water-droplet adhesiveness change in superhydrophobic anodic aluminum oxide surfaces : From highly adhesive to self-cleanable,” *Langmuir*, vol. 26, no. 3, pp. 4049–4052, 2010.
- [48] TechnicInc, “Techni copper c,” tech. rep.
- [49] N. Kanani, *Electroplating: Basic Principles, Processes and Practice*. Elsevier, 2004.
- [50] M. H. Rausch, A. Leipertz, and A. P. Fröba, “On the characteristics of ion implanted metallic surfaces inducing dropwise condensation of steam,” *Langmuir : the ACS journal of surfaces and colloids*, vol. 26, pp. 5971–5, 4 2010.
- [51] A. Leipertz and A. P. Fröba, “Improvement of condensation heat transfer by surface modifications,” *Heat Transfer Engineering*, vol. 29, pp. 343–356, 4 2008.
- [52] M. H. Rausch, A. Leipertz, and A. P. Froba, “On the mechanism of dropwise condensation of steam on ion implanted metallic surfaces,” *Journal of Heat Transfer*, vol. 132, no. 9, p. 094503, 2010.
- [53] A. Erb and R. A. Erb, “Wettability of metals under continuous condensing conditions,” *Journal of Physical Chemistry*, vol. 69, no. 4, pp. 1306–1309, 1964.
- [54] G. Azimi, R. Dhiman, H.-M. Kwon, A. T. Paxson, and K. K. Varanasi, “Hydrophobicity of rare-earth oxide ceramics,” *Nature materials*, vol. 12, pp. 315–20, 4 2013.
- [55] D. J. Preston, N. Miljkovic, J. Sack, R. Enright, J. Queeney, and E. N. Wang, “Effect of hydrocarbon adsorption on the wettability of rare earth oxide ceramics,” *Applied Physics Letters*, vol. 105, p. 011601, 7 2014.
- [56] S. Coulson, “Microfabricated devices with coated of modified surface and method of making same,” 2012.
- [57] M. R. Humphries, F. Ferdinandi, and R. E. Smith, “Halo-hydrocarbon polymer coating,” 2010.

- [58] R. J. Baumgart, M. A. Dituro, F. E. Lockwood, C. S. Phoenix, and D. E. Turcotte, "Water repellent glass treatment for automotive applications," 1999.
- [59] A. T. Paxson, J. L. Yagüe, K. K. Gleason, and K. K. Varanasi, "Stable dropwise condensation for enhancing heat transfer via the initiated chemical vapor deposition (icvd) of grafted polymer films.," *Advanced materials*, vol. 26, pp. 418–23, 1 2014.
- [60] P. Marto, D. Looney, J. Rose, and A. Wanniarachchi, "Evaluation of organic coatings for the promotion of dropwise condensation of steam," *International Journal of Heat and Mass Transfer*, vol. 29, pp. 1109–1117, 8 1986.
- [61] J. W. Rose and S. Stylianou, "Dropwise condensation on surfaces having different thermal conductivities," *Journal of Heat Transfer*, vol. 102, no. August 1980, pp. 477–482, 1980.
- [62] M.-J. Azzopardi, L. Delattre, and N. Codazzi, "Hydrophobic coating for glazing sheet," 2002.
- [63] A. Ameron and R. L. Gasmene, "Waterborne hydrophobic cleaning and coating composition," 2001.
- [64] J. F. Brown and R. A. Schneider, "Hydrophobic coating compositions, articles coated with said compositions and processes for manufacturing same," 2003.
- [65] M. Popall, J. Schulz, B.-E. Olsowski, A. Martin, and K. Buhler, "Hydrophobic coating for ink jet printing heads," 2001.
- [66] P. Shorin, "Silicone-based curable, printable hydrophobic coating compositions and processes for using the same," 1989.
- [67] R. S. Narang, S. F. Pond, D. J. Collins, and R. A. S. Harold, "Hydrophobic coating for a front face of a printhead in an ink jet printer," 1993.
- [68] E. J. Jarvholm, "Water repellent golf balls containing a hydrophobic or superhydrophobic outer layer or coating," 2008.
- [69] J. R. Smith and N. N. Garti, "Hydrophobic coating system for application to an inorganic or metallic substrate," 2000.
- [70] R. L. Gasmene, "Optically clear hydrophobic coating composition," 1995.
- [71] G. A. Dorsey, "Protective hydrophobic and oleophilic coating for aluminum products," 1978.
- [72] J. C. Love, L. a. Estroff, J. K. Kriebel, R. G. Nuzzo, and G. M. Whitesides, "Self-assembled monolayers of thiolates on metals as a form of nanotechnology," *Chemical reviews*, vol. 105, pp. 1103–69, 4 2005.

- [73] J. Maulbetsch, “Economic evaluation of alternative cooling technologies, 1024805,” tech. rep., 2012.
- [74] J. Xiong, S. Koshizuka, M. Sakai, and H. Ohshima, “Investigation on droplet impingement erosion during steam generator tube failure accident,” *Nuclear Engineering and Design*, vol. 249, pp. 132–139, 2012.
- [75] M. Bordag, A. Ribayrol, G. Conache, L. E. Fröberg, S. Gray, L. Samuelson, L. Montelius, and H. Pettersson, “Shear stress measurements on inas nanowires by afm manipulation,” *Small*, vol. 3, no. 8, pp. 1398–1401, 2007.
- [76] M. P. Manoharan and M. a. Haque, “Role of adhesion in shear strength of nanowiresubstrate interfaces,” *Journal of Physics D: Applied Physics*, vol. 42, no. 9, p. 095304, 2009.